AAEC/E453

AAEC/E453

AUSTRALIAN ATOMIC ENERGY COMMISSION

RESEARCH ESTABLISHMENT

LUCAS HEIGHTS

PROTON INDUCED X-RAY EMISSION (PIXE)
ANALYSIS AT LUCAS HEIGHTS

by

D. COHEN*
P. DUERDEN

*Australian Institute of Nuclear Science and Engineering

February 1979

ISBN 0 642 59663 8

AUSTRALIAN ATOMIC ENERGY COMMISSION
RESEARCH ESTABLISHMENT
LUCAS HEIGHTS

PROTON INDUCED X-RAY EMISSION (PIXE) ANALYSIS AT LUCAS HEIGHTS

by

D. COHEN*
P. DUERDEN

ABSTRACT

The state of the proton induced X-ray emission (PIXE) work at Lucas Heights is reported together with a full description of the experimental arrangement and its use for analysis of trace elements ($Z \geqslant 14$). The fundamentals of PIXE are examined in detail with a view to understanding not only the background continuum but also the X-ray production mechanisms. Quantitative predictions for the number of X-rays detected after proton bombardment of the target have been made and these compare well with experiments.

Australian Institute of Nuclear Science and Engineering

National Library of Australia card number and ISBN 0 642 59663 8

The following descriptors have been selected from the INIS Thesaurus to describe the subject content of this report for information retrieval purposes. For further details please refer to IAEA-INIS-12 (INIS: Manual for Indexing) and IAEA-INIS-13 (INIS: Thesaurus) published in Vienna by the International Atomic Energy Agency.

X-RAY EMISSION ANALYSIS; PROTONS; TRACE AMOUNTS; ELEMENTS; MEV RANGE 01-10; PROTON BEAMS

ERRATA

AAEC/E453

Page 4, Equation 10 *for* $e\ \bar{u}.\bar{x}$ *read* $\exp(\bar{u}.\bar{x})$

Page 25, Figure 18 *change energy levels to* keV

Page 44, Equation 26 *for* $100(1-e^{-\mu_{Si}})^{x\rho}$ *read* $(1-e^{\mu_{Si}x\rho})$

CONTENTS

1. INTRODUCTION

During the last few years, the rapid increase in interest in fast and efficient non-destructive multi-element analysis techniques has prompted the creation of a proton induced X-ray emission (PIXE) experiment at the Australian Atomic Energy Commission Research Establishment (AAECRE) at Lucas Heights. The sensitivity of this system is very high. With Kα X-rays, the minimum detectable concentrations are between 0.1 and 1 $\mu g\ g^{-1}$ for elements in the periodic range potassium to molybdenum. Since very small samples can be analysed (beam diameters can be as low as 40 μm), amounts of trace elements as low as 10^{-14} g can be detected if there is no interference from other elements.

Until the present time, the experiment has been used for many varied applications, including thorium and uranium analysis of thick ore samples, the classification of south-west Pacific obsidian and Australian tektites, the analysis of trace elements in teeth and wheat, and the authentication of ancient bronzes.

This report describes the PIXE technique and experimentation, but does not include the spectrum fitting routines for the experimental data. It is the first in a series of papers dealing with PIXE research. Section 2 describes the basic principles required for a simple understanding of the technique together with an effective approximation that has been developed for matrix corrections; Sections 3 and 5 describe the experimental arrangements; Section 4 is a comprehensive appraisal of the PIXE spectra and includes details of the origins of background and peak components of the spectra; and Section 6 discusses sensitivity of the system and the minimum detectable concentrations.

2. BASIC PRINCIPLES

With the advent of high-resolution semiconductor detectors (SiLi and GeLi), the time required for multi-element analysis by the PIXE technique has been greatly reduced as many elements can now be detected simultaneously.

When the sample is bombarded with a projectile producing ionisation of the inner atomic shells, characteristic X-rays are emitted and can be observed. The lifetime of an electron vacancy is $\sim 10^{-15}$ s in a solid target.

The interaction of the charged particle and the target atom is coulombic and its major features are well understood. Generally, the

plane wave Born approximation (PWBA) is used to treat inner shell ionisation by protons. This approach explains quantitatively the dependence of ionisation cross sections at high particle energies whereas, in the lower energy region, corrections for binding energy of the target atom electrons and the coulomb scattering of the particle must be considered in order to obtain a quantitative description of the process.

The binary encounter model is also sometimes used. This accounts best for points corresponding to lower Z values, whereas for higher Z values, in which the cross sections vary more rapidly, the PWBA is best.

The ionisation cross section increases with proton energy E_p and reaches a maximum for K,L X-rays in a given target element when

$$E_p \approx \frac{M_p}{m_e} \cdot E_{K,L} \quad ,$$

where the velocity of the proton approximately equals the mean velocity of the K,L shell electron of binding energy $E_{K,L}$.

2.1 X-ray Production Cross Section

The X-ray production cross section σ_X is related to the ionisation cross section σ_I for a line in a spectrum by

$$\sigma_X = \sigma_I \, w_{K,L}{}^k \quad , \qquad (1)$$

where $w_{K,L}$ is the fluorescence yield for a K or L shell vacancy and k is the relative line intensity of possible transitions to fill an inner shell vacancy.

Reuter *et al.* [1975] calculated K shell fluorescence yields from an empirical fit to the experimental data of Bambynek *et al.* [1972]:

$$\left[\frac{w_K}{1-w_K}\right]^{\frac{1}{4}} = 0.015 + 0.0327\ Z - 0.64 \times 10^{-6}\ Z^3 \qquad (2)$$

Table 1 includes values of $w_{K,L}$ and k for the proton energy E_p and atomic number Z.

Johansson & Johansson [1976] summarised recent measurements of one X-ray production cross section in the 0.5 to 10 MeV proton energy range. These values are reproduced in Table 1. The experimental cross section values are generally good to within 10-30 per cent in the energy and Z regions of interest. In the same paper all the experimental data has been fitted to a 5th degree polynomial.

TABLE 1

Kα AND L X-RAY PRODUCTION CROSS SECTIONS

[After Johansson & Johansson 1976]

(i) Kα X-ray production cross sections (barns)

Element	Z	ω_K[a]	K_β/K_α[b]	Proton energy (MeV) 0.5	1.0	1.5	2.0	2.5	3.0	3.5	4.0	4.5	5.0	6.0	7.0	8.0	9.0	10.0
Al	13	0.0357	0.0134	219	625	906	1054	1113	1120	1100	1066	1027	985	910	847	797	–	–
S	16	0.0761	0.0659	68.2	257	473	638	736	832	877	899	905	900	873	834	792	753	717
Ca	20	0.163	0.1315	15.2	80.3	174	274	366	446	511	564	604	634	671	684	682	672	657
Ti	22	0.219	0.1355	7.51	45.2	106	176	248	315	374	425	469	504	556	586	601	606	603
Cr	24	0.282	0.1337	3.79	25.7	64.5	113	166	218	268	313	354	389	446	486	512	527	535
Fe	26	0.347	0.1391	1.90	14.5	38.6	70.9	108	146	185	222	256	287	341	383	414	436	451
Ni	28	0.414	0.1401	0.961	8.25	23.3	44.5	69.9	97.6	126	155	182	209	256	295	327	352	371
Zn	30	0.479	0.1410	0.485	4.69	14.0	27.7	44.8	64.2	85.0	106	128	148	187	222	251	275	295
As	33	0.567	0.1560	0.168	1.96	6.32	13.2	22.3	33.0	45.0	57.8	71.1	84.5	111	136	159	179	197
Br	35	0.622	0.1683	0.0829	1.10	3.75	8.11	14.0	21.2	29.4	38.4	47.9	57.7	77.6	97.1	116	133	148
Sr	38	0.691	0.1831	0.0284	0.466	1.72	3.90	6.98	10.9	15.4	20.6	26.2	32.1	44.6	57.4	70.0	82.2	93.6
Mo	42	0.764	0.1981	0.00678	0.151	0.621	1.50	2.81	4.53	6.63	9.07	11.8	14.8	21.3	28.3	35.6	42.9	50.0
Ag	47	0.830	0.2130	0.00111	0.0376	0.180	0.472	0.932	1.57	2.37	3.34	4.45	5.71	8.56	11.8	15.3	18.9	22.7
Sn	50	0.859	0.2230	–[c]	0.0163	0.0862	0.238	0.487	0.839	1.29	1.85	2.51	3.25	4.98	6.99	9.21	11.6	14.1
Ba	56	0.901	0.2433	–	0.00310	0.0203	0.0626	0.137	0.249	0.399	0.589	0.818	1.09	1.73	2.51	3.41	4.41	5.49
Pb	82	0.968	0.2821	-	–	–	0.246 (−3)	0.799 (−3)	0.00189	0.00370	0.00638	0.0100	0.0148	0.0278	0.0458	0.0692	0.0979	0.132

a 'Fitted' values from Bambynek *et al.* [1972] *b* Scofield [1974] *c* '-' denotes value outside range of formal validity

(ii) L X-ray production cross sections (barns)

Element	Z	$\overline{\omega_L}$[a]	Proton energy (MeV) 0.5	1.0	1.5	2.0	2.5	3.0	3.5	4.0	4.5	5.0	6.0	7.0	8.0	9.0	10.0
Zn	30	0.0059	576	1253	1678	1917	2038	2086	2086	2058	2012	1956	1828	–[b]	–	–	–
Br	35	0.020	450	1212	1836	2292	2609	2823	2960	3041	3080	3089	3046	2954	2839	2713	2584
Zr	40	0.031	175	572	965	1299	1569	1782	1947	2072	2165	2233	2310	2332	2319	2283	2232
Ag	47	0.060	60.5	250	479	704	910	1092	1251	1386	1502	1599	1749	1851	1916	1954	1972
Sn	50	0.079	39.0	178	359	546	725	889	1036	1167	1282	1383	1545	1665	1752	1812	1851
Ba	56	0.120	15.0	83.3	185	300	418	534	643	746	840	927	1077	1200	1300	1379	1442
Gd	64	0.19	4.47	31.8	79.5	139	206	275	344	412	478	541	677	760	850	928	996
Hf	72	0.26	1.26	11.5	32.2	60.7	94.5	132	170	210	250	289	365	437	503	563	617
W	74	0.30	0.981	9.53	27.5	52.8	83.3	117	153	190	227	265	338	407	471	531	585
Au	79	0.34	0.421	4.80	14.9	30.0	48.8	70.4	93.9	119	144	170	222	272	320	366	408
Pb	82	0.38	–	3.3	10.7	22.2	36.8	53.8	72.7	92.7	114	135	179	222	263	303	341
U	92	0.50	–	0.876	3.32	7.53	13.4	20.5	28.9	38.1	48.0	58.5	80.7	104	127	150	173

a Estimated from Bambynek *et al.* [1972 : Figures 4-34] *b* '-' denotes value outside range of formal validity

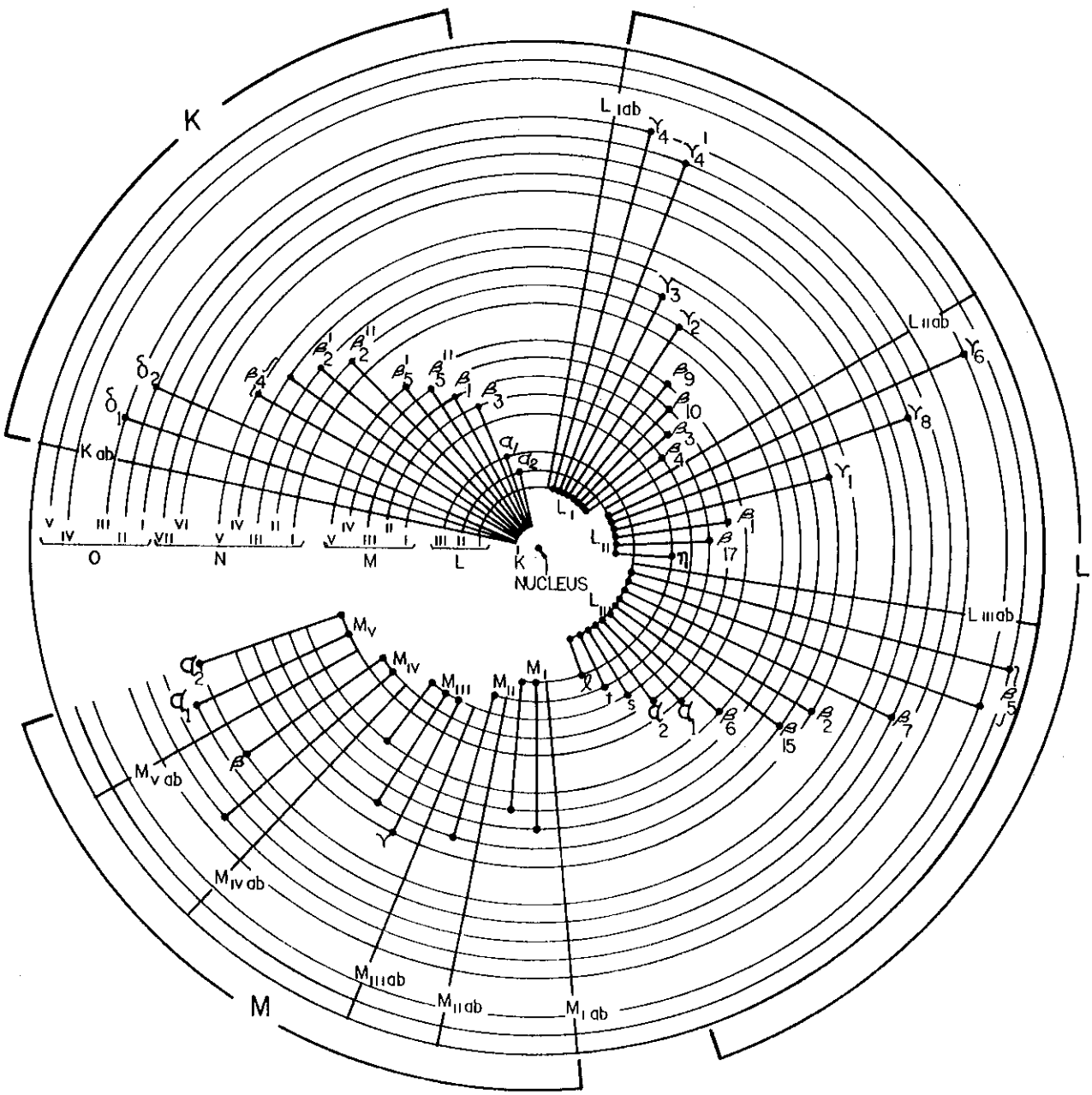

Figure 1 Possible Electron Transitions Following Electron Vacancies

$$\ell n(\sigma_I E_I^2) = \sum_{n=0}^{5} b_n x^n \quad , \tag{3}$$

where $$x = \ell n \left[\frac{10^3 E_p}{\lambda E_I} \right] \quad , \tag{4}$$

$$\lambda = M_p/m_e = 1836 \quad , \tag{5}$$

E_p = energy of proton in MeV,

E_I = ionisation energy in keV of ith (I = K or L) shell,

σ_I = ionisation cross section in units 10^{-14} cm^2,

b_n are coefficients given in Table 2,

E_L is calculated from the three L absorption edges, and

$$E_L = \frac{1}{4} (E_{L1} + E_{L2} + 2E_{L3}) \tag{6}$$

TABLE 2

COEFFICIENTS OF LEAST SQUARES FIT, b_i

	b_0	b_1	b_2	b_3	b_4	b_5
K	2.047	-0.06591	-0.4745	0.09919	0.04606	0.00609
L	3.608	0.3712	0.3712	-0.0000786	0.00251	0.00126

A one sigma confidence interval for the experimental ionisation cross sections about this polynomial fit is better than 5 per cent for the K X-rays and 8 per cent for the L X-rays over the general proton energy and Z range of interest. A complete level scheme for electron transitions into inner shell vacancies is shown in Figure 1. Some transitions are not resolved because of the finite detector resolution.

For K shell vacancies only two possible lines have been considered:

$K\alpha \equiv K(\alpha_1+\alpha_2)$ is L_{II}, $L_{III} \rightarrow K$

$K\beta \equiv K(\beta_1+\beta_2+\beta_3)$ is M_{III}, N_{II}, N_{III}, $M_{II} \rightarrow K$

For L shell vacancies the lines are as follows:

$L\alpha_1$ $M_V \rightarrow L_{III}$

$L\alpha_2$ $M_{IV} \rightarrow L_{III}$

$L\beta_1$ $M_{IV} \rightarrow L_{II}$

$L\beta_2$ $N_V \rightarrow L_{III}$

$L\beta_3$ $M_{III} \rightarrow L_I$

$L\beta_4$ $M_{II} \rightarrow L_I$

$L\gamma_1$ $N_{IV} \rightarrow L_{II}$

$L\gamma_3$ $N_{III} \rightarrow L_I$

$L\ell$ $M_I \rightarrow L_{III}$

$L\eta$ $N_I \rightarrow L_{II}$

and for M shell vacancies the lines are

$M\alpha$ $N_{III} \rightarrow M_V$

$M\beta$ $N_{VI} \rightarrow M_{IV}$

2.2 Relative Line Intensities

The $K\beta/K\alpha$ line intensity ratio for elements from calcium upwards, and L line intensities of $L\alpha$ for selected elements from lanthanum upwards, have been measured; the measured $K\beta/K\alpha$ ratios (with 100 per cent detector efficiency) are shown in Figure 2 with the theoretical calculations of Scofield [1974] superimposed for comparison. All the features of the theoretical curve are well reproduced. Our mean measured value for the Z = 20 to 30 plateau is

$$\frac{K\beta}{K\alpha} = 0.143 \pm 0.023 \quad .$$

This fixed value has been used for all PIXE fitting and unfolding routines performed at Lucas Heights [Clayton *et al.* AAEC report in preparation] in the Z range 20 to 30. Since our measurable Z region is in excellent agreement with that of Scofield, we have used his $K\beta/K\alpha$ ratios to extend the data into the unresolved $Z \lesssim 20$ region. The values of $(K\beta/K\alpha)$ used for Z = 13 to 50 and relative L line intensities are shown in Table 3, and measured $L\alpha/K\alpha$ and $M\alpha/L\alpha$ data are given in Figure 2.

2.3 Quantitative Analysis

For a thin target, the basic equation used to calculate the number of X-rays in a peak produced by a certain element in the sample is

$$N_T^{thin} = \frac{A\, n_p\, \sigma_X\, \Omega\epsilon}{4\pi} \quad , \qquad (7)$$

where A is the number of atoms of the trace element per cm^2 of target;

TABLE 3

RELATIVE LINE INTENSITIES

Element	Z	Kβ/Kα	
		Scofield	Cohen + Duerden
Al	13	0.0134	
Si	14	0.0294	
P	15	0.0472	
S	16	0.0659	
Cl	17	0.0862	
Ar	18	0.1088	
K	19	0.1211	
Ca	20	0.1315	
Ti	22	0.1355	0.132
V	23	0.1367	
Cr	24	0.1337	
Mn	25	0.1385	0.144
Fe	26	0.1391	0.149
Ni	28	0.1401	0.159
Cu	29	0.1379	0.147
Zn	30	0.1410	0.152
Ge	32	0.1504	
As	33	0.1560	
Se	34	0.1629	
Br	35	0.1683	
Kr	36	0.1727	
Rb	37	0.1780	
Sr	38	0.1831	0.185
Zr	40	0.1913	0.181
Mo	42	0.1981	0.207
Ag	47	0.2130	0.202
Sn	50	0.2230	0.203
Sb	51	0.2266	0.206
Xe	54	0.2368	
Ba	56	0.2433	0.234
La	57		
Nd	60	0.2504	

Element	Z	Relative Intensities						
		Lℓ	Lα	Lη	Lβ1	Lβ2	Lγ1	Lγ3
Ag	47	0.042	1.000	0.08	0.4	0.3	0.1	0.05
Ba	56	0.032	1.000	0.1	0.69	0.28	0.058	0.025
La	57	0.030	1.000		0.74	0.29	0.05	0.025
Dy	66	0.04	1.000		0.52	0.22	0.097	0.025
Lu	71	0.04	1.000	0.03	0.46	0.24	0.089	0.016
Ta	73	0.035	1.000		0.43	0.24	0.05	0.015
Pb	82	0.040	1.000	0.015	0.707		0.07	0.015
Th	90	0.069	1.000	0.016	0.231	0.298	0.05	0.014
U	92	0.069	1.000	0.016	0.231	0.255	0.05	0.014

n_p is the total number of protons hitting the target;

σ_X is the cross section for X-ray production for the peak;

Ω is the solid angle subtended by the target at the detector (steradians); and

ε is the detector efficiency (including all the absorption effects).

If N_X is defined as the number of X-rays atom^{-1} sr^{-1} (μC cm^{-2})$^{-1}$ of incident protons, then Equation (7) becomes

$$N_T^{thin} = AN_X (It)\ \Omega\varepsilon \quad , \tag{8}$$

where It is the total charge hitting the target in μC.

Figure 3 is a plot, taken from Deconninck *et al.* [1975], of N_X versus incident proton energy E_p for K and L series X-rays. The cross sections used to produce these curves were taken from the calculations of Gordon & Kraner [1972]. The detector was made of 3 mm thick SiLi with a 25 μm Be window having 100 per cent efficiency over the $4 < E_X < 20$ keV X-ray region.

We have shown in Appendix A that the total X-ray yield for a thin target is

$$N_T^{thin} = 600\ N_X (It) \left[\frac{C}{W}\right] \Omega\varepsilon \quad , \tag{9}$$

where N_X is in units of 10^{-12} atom^{-1} sr^{-1} (μC cm^{-2})$^{-1}$;

It is the total charge hitting the target in μC;

C is the trace element concentration in μg g^{-1};

W is the atomic weight of the trace element;

and a thin target was defined as being 1 mg cm^{-2} thick.

For thicker targets, the protons are slowed down, thus changing the cross section for X-ray production, and some of the X-rays induced may be absorbed in the sample material (matrix). An integration of Equation (7) with the proton energy E_p is required, giving

$$N_T^{thick} = n_p \frac{\Omega\varepsilon}{4\pi} \int_{E_p}^{o} \sigma_X \frac{N_A\ dE\ e^{\bar{\mu}.\bar{x}}}{W\ S(E)} \quad , \tag{10}$$

where N_A is Avogadro's number,

$S(E)$ is the stopping power of the target material,

$\bar{\mu}.\bar{x}$ is the outgoing X-ray attenuation factor in the target, and

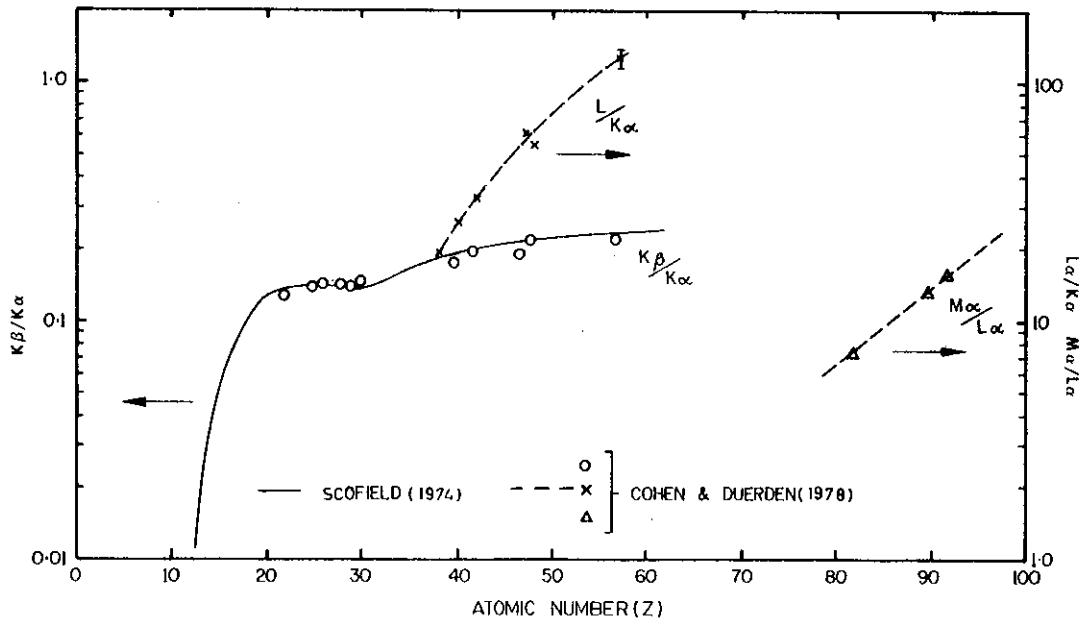

Figure 2 Kβ/Kα L/Kα and Mα/Lα Ratios *versus* Z

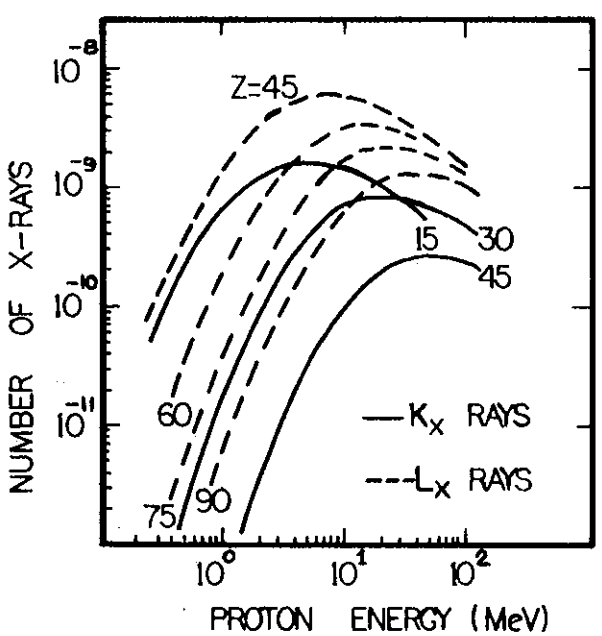

Figure 3 Number of K and L X-rays Produced *versus* Proton energy

$$\bar{\mu}.\bar{x} = \mu \int_{E_p}^{E} \frac{dE}{S(E)} \cdot \frac{\cos \theta_i}{\cos \theta_o} \quad ,$$

where μ is the mass absorption coefficient of the target material at the X-ray energy, and

θ_i, θ_o are the angles of the incident protons and the outgoing X-rays, respectively (both 45° in this case), measured to the normal of the target surface.

The integrals of Equation (10) must generally be calculated numerically on a computer with reference to stopping power and mass absorption coefficient tables.

Figures 4 and 5 show the stopping power and proton range versus proton energy, and the mass absorption coefficient versus X-ray energy for various target matrices. The complex nature of these plots makes an approximation to the integrals necessary. Hence an effective active matrix volume has been defined for X-ray production.

2.4 Effective Active Volume of Target

It can be shown that half the total X-ray production occurs in the first quarter of the proton range [Deconninck *et al.* 1975]. The assumption is made that *all* the X-rays are produced in a thin layer at a depth equal to one quarter of the proton range R. Using this approximation, the total number (N_T^{approx}) of X-rays detected in a peak has been calculated (see Appendix A):

$$N_T^{approx} = 15\, N_X (It) \left[\frac{C\rho R}{W}\right] \left[\exp(-2.5 \times 10^{-5}\, \mu\rho R)\right] \Omega\varepsilon \quad , \qquad (11)$$

where ρ is the density of the matrix in g cm^{-3}, and

R is the range of proton in the matrix in μm.

Values for ρR versus Z of the matrix for different proton energies are shown in Figure 6. The transmission factor (the second square bracket of Equation (11)) is plotted as a function of X-ray energy in Figure 7. Figures 3, 6 and 7 enable the determination of N_T^{approx} from Equation (11).

For example, consider 100 μg g^{-1} Zn in a carbon matrix bombarded by 2.4 MeV protons at 100 nA for 1000 s (100 μC). Then

$C = 100\ \mu g\ g^{-1}$,

$\rho = 2.25\ g\ cm^{-3}$, $R = 51\ \mu m$ } $\rho R = 115$ (see Figure 6),

$W = 65$ for Zn,

$N_X = 1.2 \times 10^{-10}\ atom^{-1}\ sr^{-1}\ (\mu C\ cm^{-2})^{-1}$,

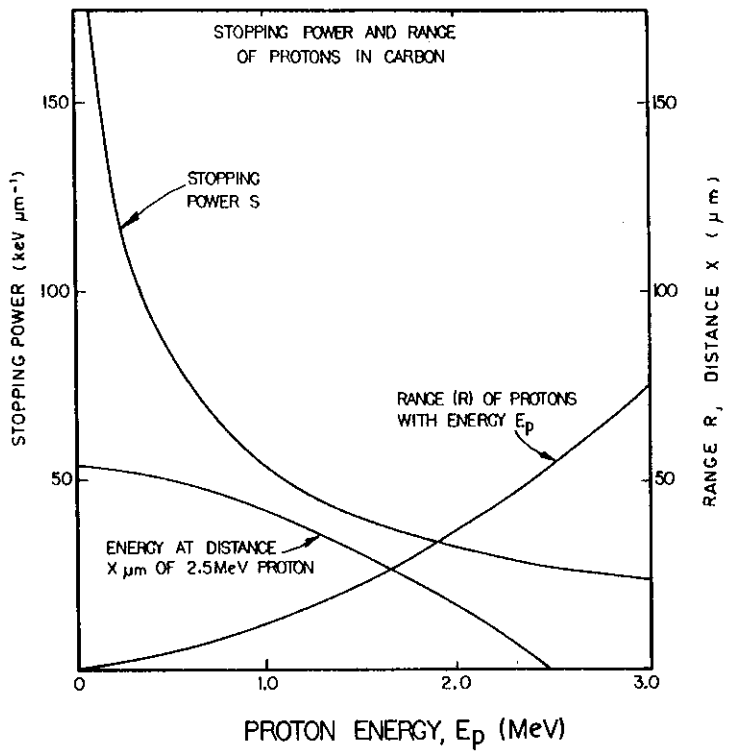

Figure 4 Stopping Power and Range of Protons in Carbon

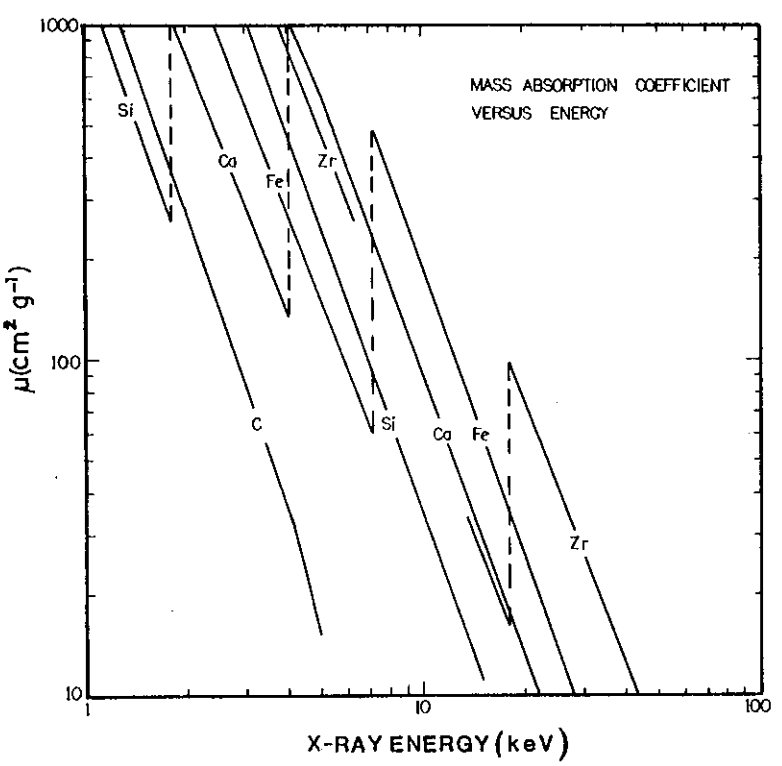

Figure 5 Mass Absorption Coefficient *versus* Energy

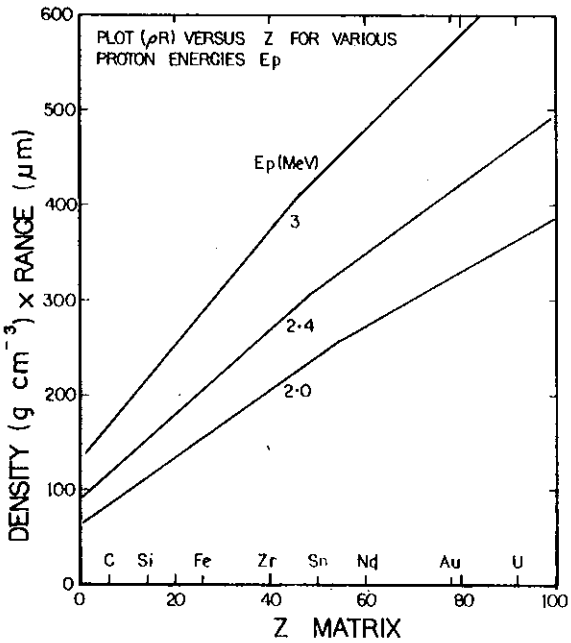

Figure 6 Density x Range *versus* Z of Matrix

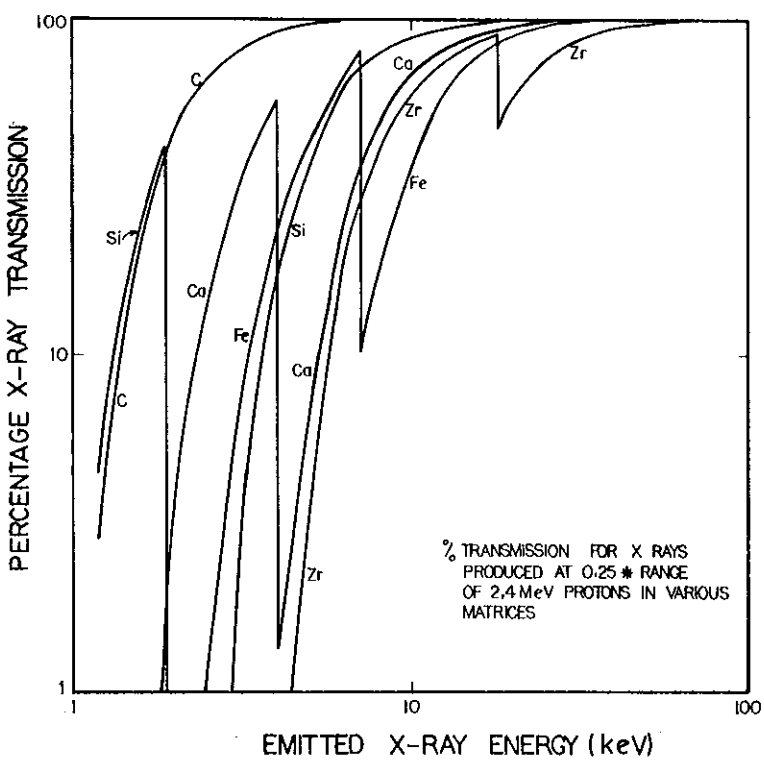

Figure 7 X-ray Percentage Transmission *versus* Emitted X-ray Energy in Various Matrices

Ω = 4×10^{-4} sr (for a 10 mm^2 detector placed 15 cm from the target),

It = 100 μC,

$[e^{-\mu\rho R/4}]$ = 0.99. From Figure 7 for Zn Kα, 8.6 keV X-rays,

ε = 0.97 for the Zn Kα X-ray, and

N_T = 12 200 counts in the Zn K peaks.

This compares very well with our experimentally measured value of 12 800 counts obtained from the sensitivity curves discussed in Section 6.

2.5 Matrix Optimisation

Figures 8a and 8b give plots of N_T^{approx} per 100 μg g^{-1} per 100 μC versus Z of the trace element in various matrices, for K and L X-rays respectively; all elements from Z = 15 upwards are dealt with. It can be seen in both figures that there is a region of high sensitivity if $E_X < E_{Kabs}$ of the matrix.

For a given trace element, proton energy and fixed detector geometry, Equation (11) has a maximum when

$$2.5 \times 10^{-5}\ \mu\rho R = 1$$

or $$\mu\rho R = 4 \times 10^4 \quad .$$

For a given matrix then, it is possible to find the trace element that maximises the total X-ray count, as is shown quite clearly on the plots in Figure 8. Figure 9 shows a plot of the trace element Z versus the matrix Z that maximises the X-ray count N_T^{approx}. Inclusion of the detector efficiency moves the maxima for a given Z of the matrix to a higher trace element Z. This is shown as the dashed curves in Figure 9.

2.6 Correction Factors

Having found a reasonable approximation to the thick target situation, a correction factor F can be defined as

$$F = \frac{N_T^{thin}}{N_T^{approx}} = \frac{40}{\rho R}\,[\exp(2.5 \times 10^{-5}\ \mu\rho R)] \quad . \qquad (12)$$

F is plotted in Figure 10 as a function of the trace element Z for various matrices. For lower Z, it rises very steeply and requires quite large thick target corrections. However for high X-ray energies travelling in light Z matrices, F has an asymptotic value $F_o = 40/\rho R$; F_o is not unity since the assumption has been made that a thin target is 1 mg cm^{-2} thick. The real correction factor of interest then is F/F_o which is the reciprocal of the transmission factor discussed in Section 2.4

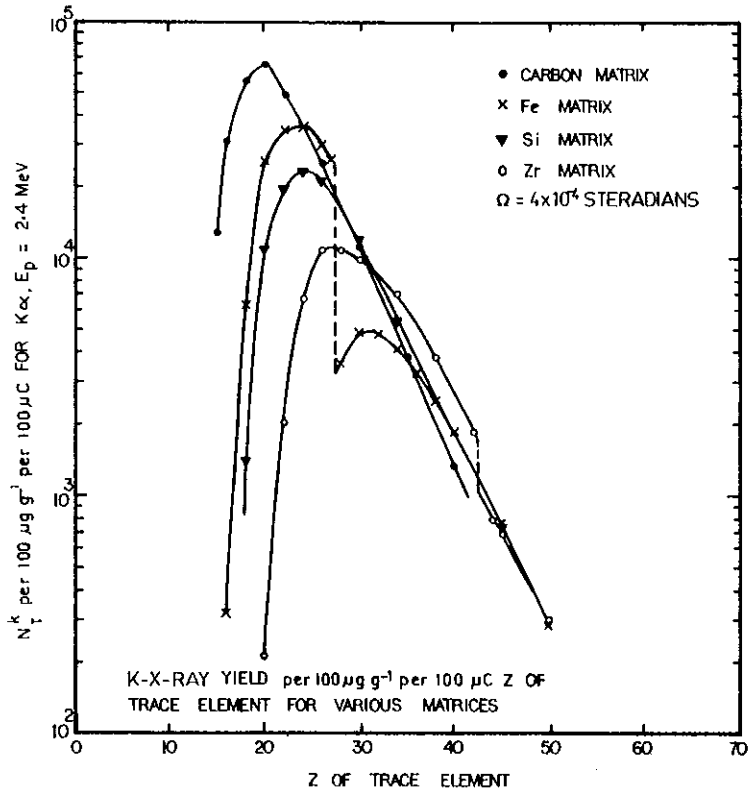

Figure 8a Total K X-rays Detected for Trace Element in Various Matrices

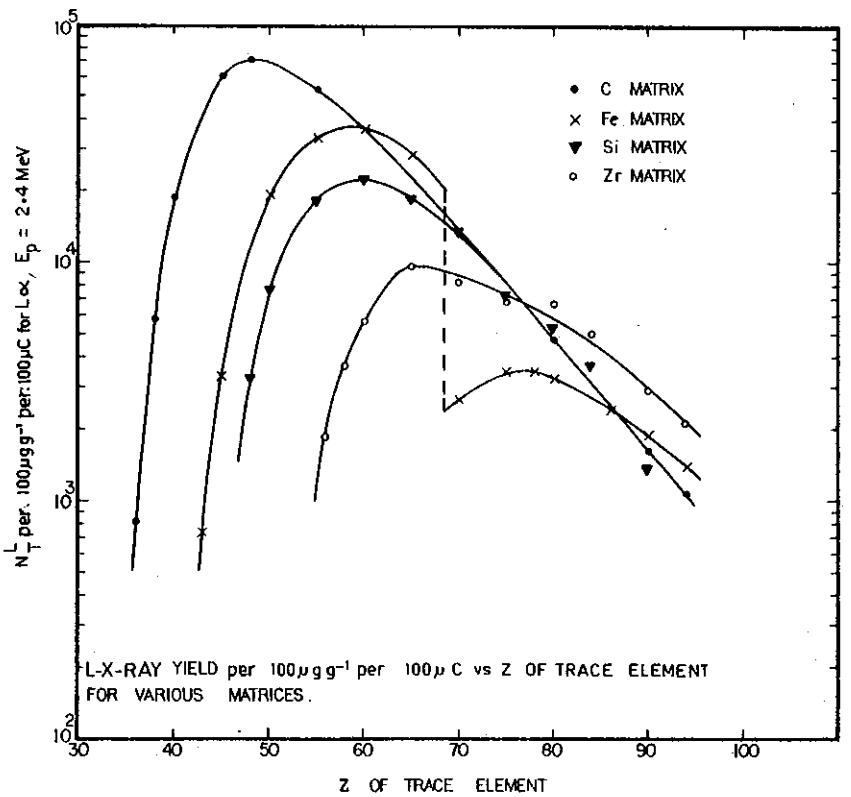

Figure 8b Total L X-rays Detected for Trace Element in Various Matrices

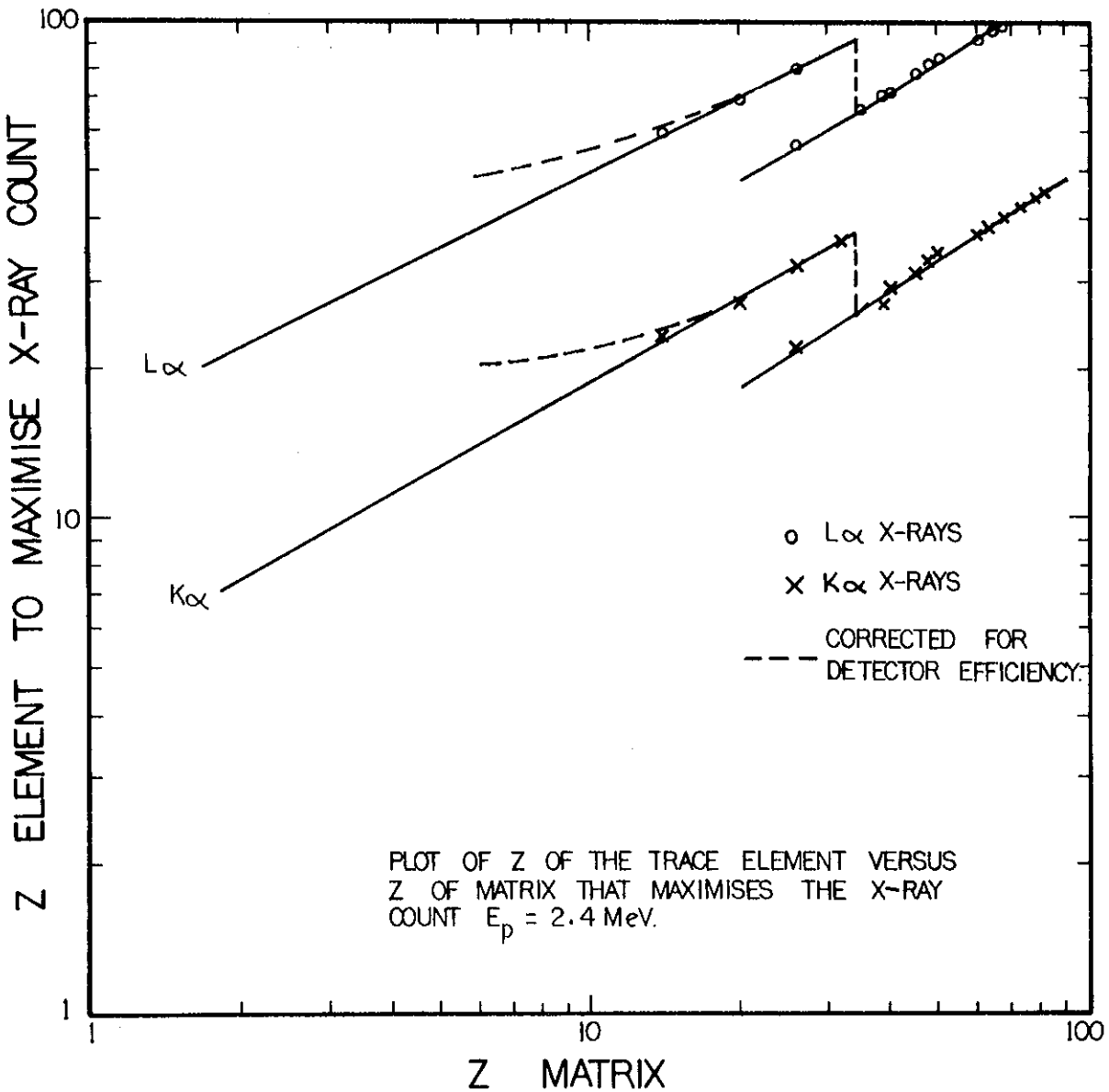

Figure 9 Optimum Matrix for Trace Element Analysis

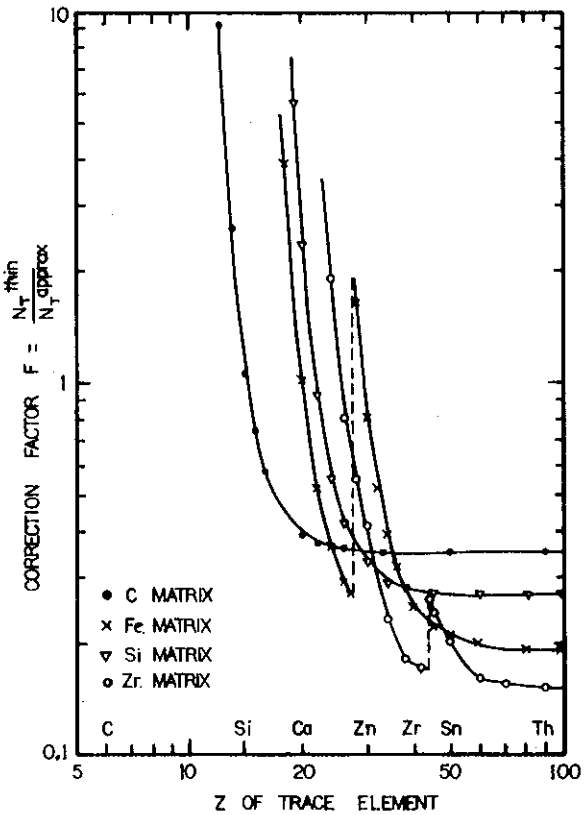

Figure 10 Correction Factors *versus* Z

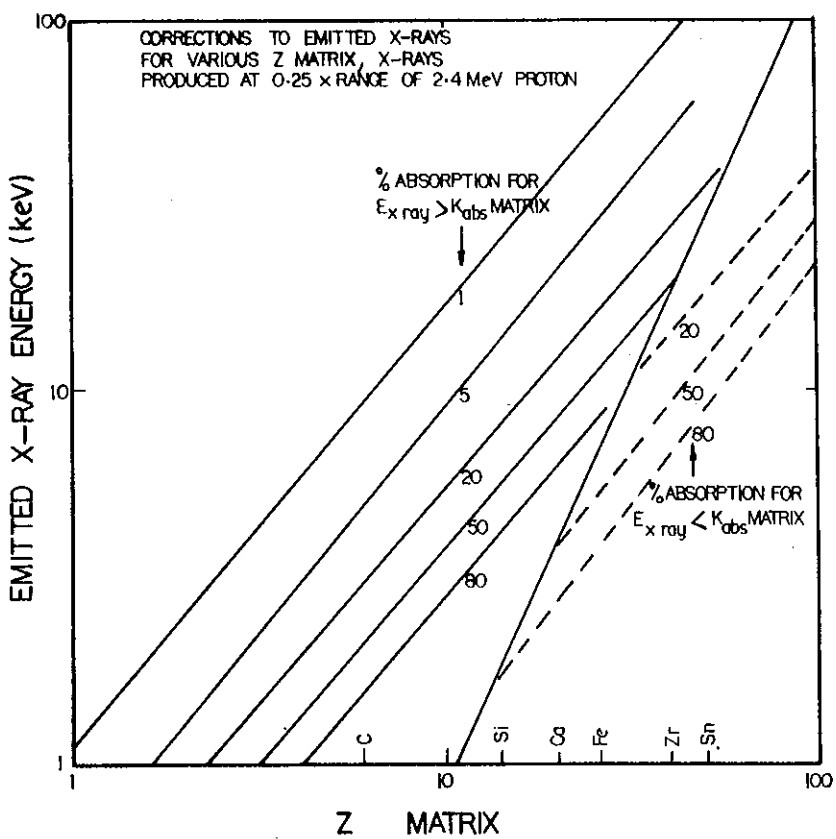

Figure 11 Absorption Corrections for Emitted X-rays in Various Matrices

and plotted as a function of X-ray energy in Figure 7.

Figure 11 gives the magnitude $(1-F_o/F)$ of the X-ray absorption correction necessary for a given X-ray energy in a given matrix background. Correction factors for thick targets have been calculated (using our approximation) and compared with thick target results of Deconninck *et al.* [1975] over the X-ray energy range $4 < E_X < 20$ keV. There is better than 20 per cent agreement between the results for all the thick targets over this X-ray energy range.

3. EQUIPMENT

The experimental arrangement at Lucas Heights is shown in Figure 12. The 3 MeV Van de Graaff accelerator is used to produce protons with energies in the range 2 to 3 MeV. These are steered through an energy analysing magnet and a diffusing quadrupole onto an aperture whose size can be varied between 0.1 and 9 mm diameter. The target chamber is insulated ($\gtrsim$ 70 MΩ) from the rest of the experiment and thus acts as a Faraday cup for charge collection and integration to give a measure of the total current reaching the target. Many targets can be placed on a metre long stick, whose position in the incident proton beam is varied, to an accuracy of ± 100 μm, by a computer-controlled stepping motor.

A carbon filament attached to the top of the chamber is used to flood insulated targets with electrons. The target chamber is kept at a base pressure of ~ 0.5 mPa. At the base of the chamber there is a 25 μm beryllium window above the detection system. X-rays produced in the target can be selectively absorbed by filters (usually 1.5 mm layers of Perspex) placed between the bottom of the chamber and the detector. The detector sits on a platform of adjustable height, therefore the column of air (which also acts as a filter for low energy X-rays) between the chamber and the top of the detector can be varied from about 20 cm down to a few millimetres.

3.1 The Detector

The detector, built at Lucas Heights by Beech & Eberhardt [1973], has the following characteristics:

- Intrinsic hyper-pure n-type silicon of resistivity 90 kΩ cm.
- Active area, 50 mm^2.
- Depletion thickness, 5 mm.
- Front contact, ~ 10 nm of vacuum-evaporated gold.
- Bias voltage, 1400 to 1650 V negative.

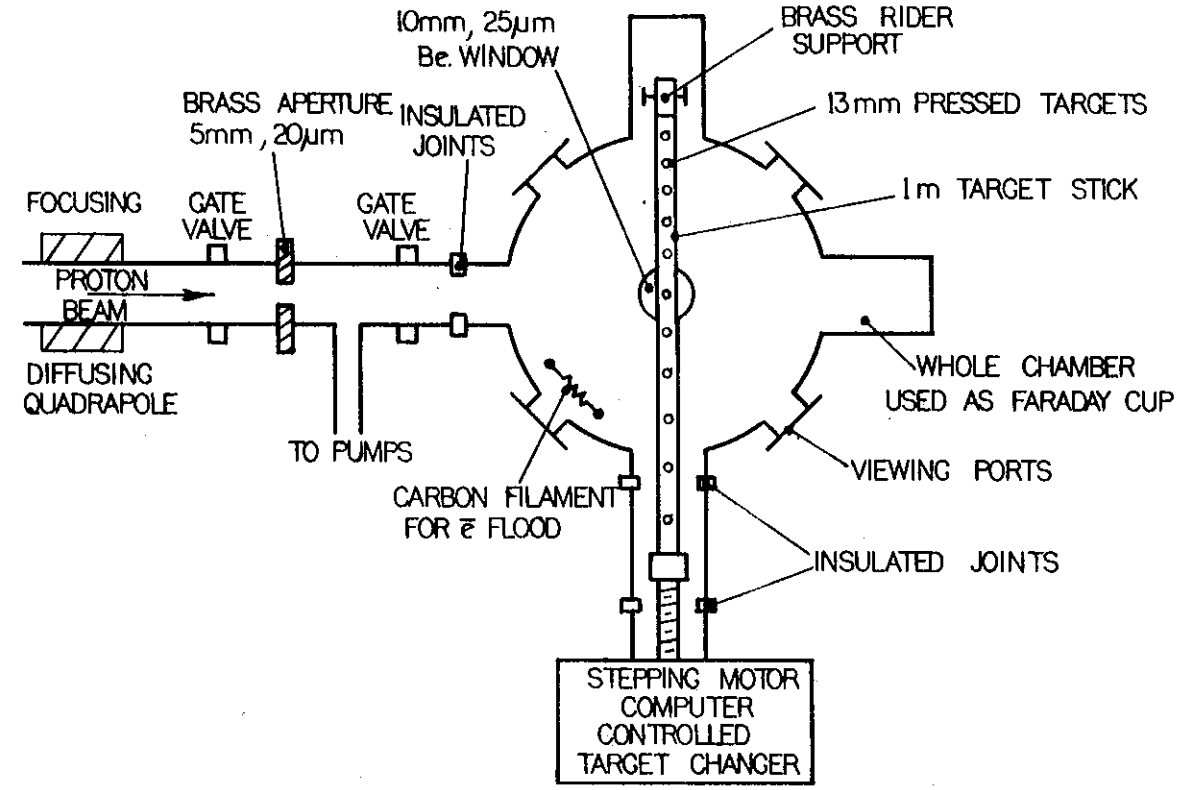

PIXE CHAMBER TOP VIEW

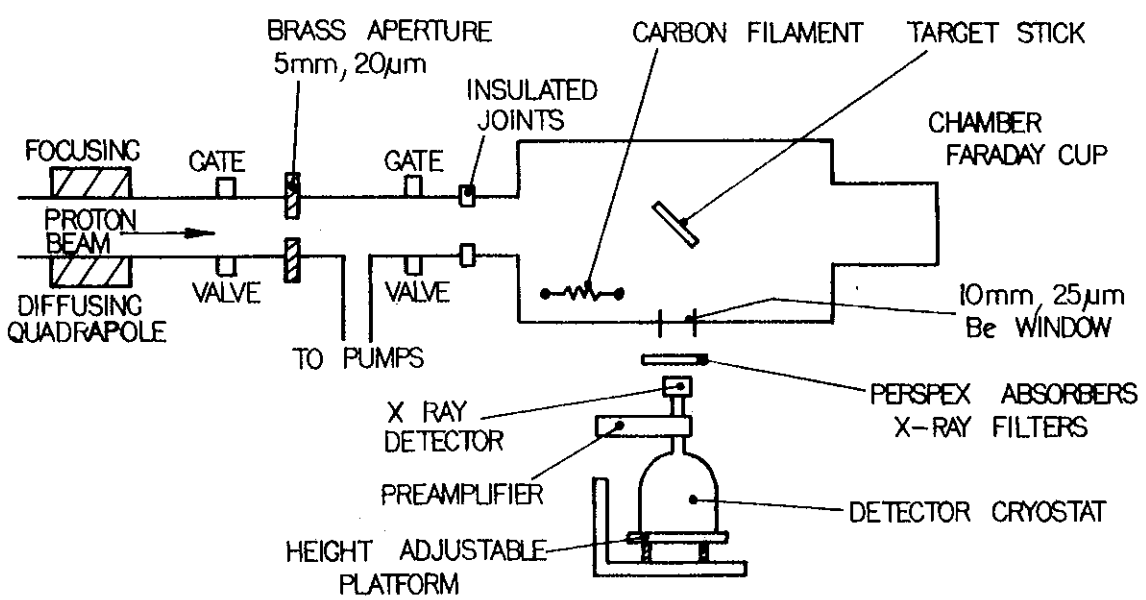

PIXE CHAMBER SIDE VIEW

Figure 12 Experimental Arrangement

. Detector window, 25 μm Be.

. Operating temperature, 77 K (liquid nitrogen cooled).

A low energy X-ray entering the semiconductor detector is totally absorbed and loses its energy by producing free charge carriers (*i.e.* electron hole pairs in the semiconductor) and lattice phonons. The carriers, the numbers of which are proportional to the energy of the X-ray, move under the influence of the electric field until they are collected at the electrodes or trapped internally by the crystal. Each ionisation event in the detector requires 3.81 eV of energy from the X-ray, hence the total collected charge, Q, is

$$Q = \frac{E_x(\text{keV})}{3.81 \times 10^{-3}} \; 1.6 \times 10^{-19} \; \text{C} \; .$$

The high resolution of the detector is a consequence of the high precision in the energy-to-charge conversion. A large number of electron hole pairs results from a given energy deposit E_X yielding excellent statistical definition of the 'size' of the charge pulse.

To reduce detector leakage current and surface recombination losses of charge carriers, a guard ring is used to define the boundary of the sensitive region rather than a physical surface with its unknown charge-trapping characteristics. This reduces low energy tailing and detector background by a factor of at least 10.

3.1.1 Detector resolution

There are two main contributors to the Full Width Half Maximum (FWHM) of the peaks:

$$(\text{FWHM})^2 = \Delta^2_{\text{electronic}} + 2.355^2 \; (F\epsilon E) \qquad (13)$$

where $\Delta_{\text{electronic}}$, the width associated with the electronics, is a function of the main amplifier shaping time; the Fano factor, F, takes account of the statistical shaping of the proton energy between charge and phonon productivity and has a value between 0 and 1. In this detector, it has the value 0.11 ± 0.04 [Musket 1974]; ϵ = 3.81 eV is the average energy required to form an electron-hole pair; and E_x is the photon energy.

The electronic component of the FWHM for our detector was measured at 6 μs shaping time and found to be 260 ± 10 eV; the FWHM versus incident photon energy calculated with this value for $\Delta_{\text{electronic}}$ is shown in Figure 13.

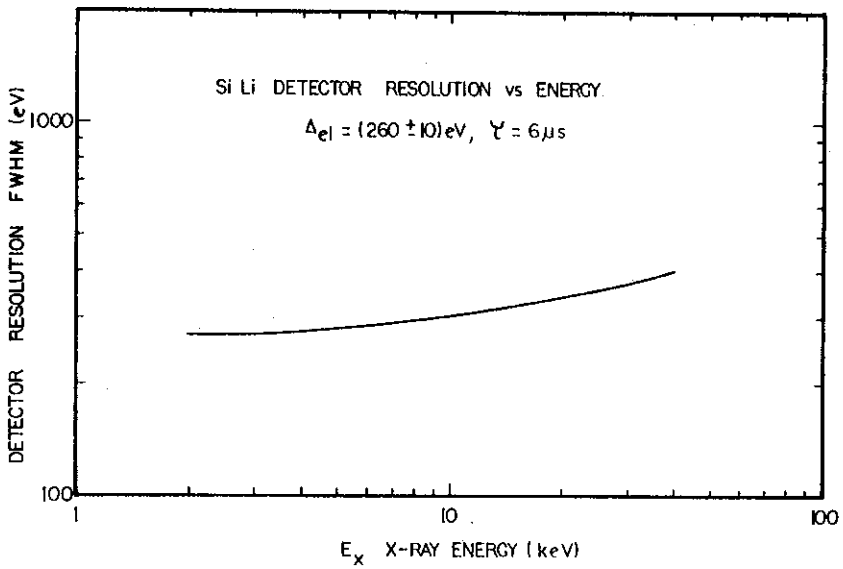

Figure 13 Detector Resolution

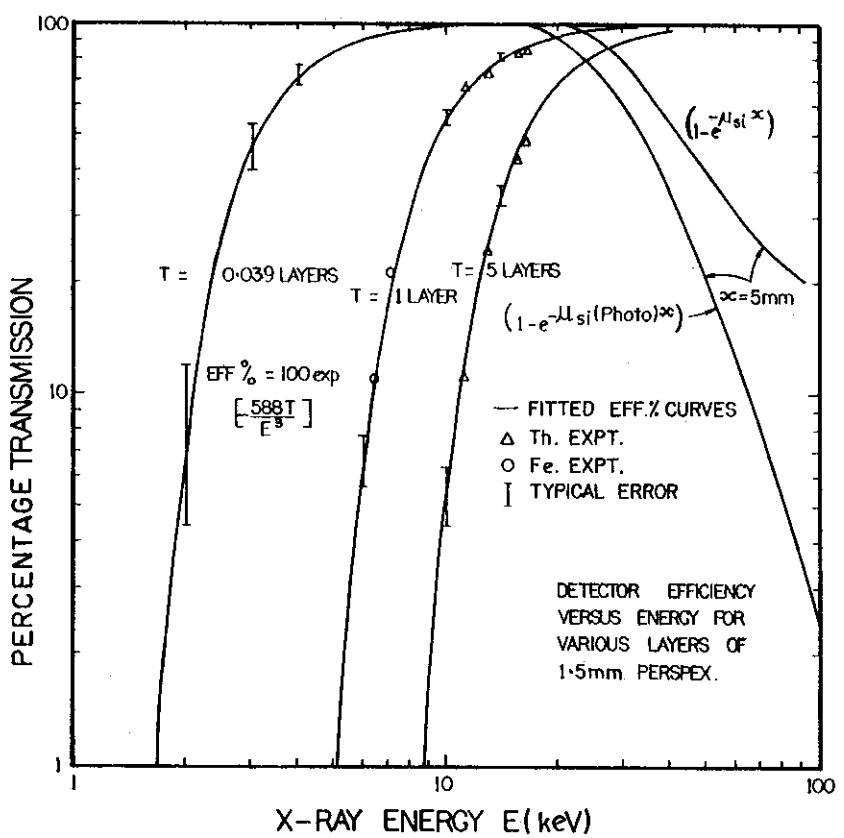

Figure 14 Detector Efficiency with Perspex Filters

3.1.2 Detector efficiency

At low X-ray energies, the detector efficiency is determined mainly by the nature of the absorbing layers between the target and the detector surface. In the present case, these include two 25 μm Be windows, three centimetres of air and a thin (~ 10 nm) Au layer on the surface of the detector. The detector efficiency has been calculated for the zero filter case (see Section 5). At low energies (E_x < 3 keV), the main contribution to the X-ray absorption comes from the 3 cm air gap. If this air gap were replaced with a vacuum, the detector would be ~ 20 per cent efficient at 1.55 keV instead of only ~ 0.4 per cent. However, for most work above 6 keV this is not a problem and the convenience of being able to insert filters as required between the detector and the target is an advantage.

A dip of the order of 2 per cent in the detector efficiency could be expected at the silicon K absorption edge 1.839 keV; however, because of the low efficiency (< 10 per cent) of the detector in this region, little work has been done to verify this.

At high X-ray energies, the full energy efficiency becomes a function of the thickness of the active volume and its effectiveness in completely absorbing the photon. This has a $(1-\exp(\mu_{si}x))$ dependence, where $\mu_{si} = \mu_{si}$ (photo) + μ_{si} (Compton) + μ_{si} (pair production) is the total linear mass absorption coefficient for silicon, and x is the depletion thickness of the detector (5 mm). The detector efficiency dependence on X-ray energy is shown in Figure 14. The photo peak efficiency is better than 80 per cent over the energy range 8 < E_x < 24 keV; this includes Kα X-rays from the elements Cu to Sn and Lα X-rays for elements from W upwards. For the complete Z range from Ca upwards, the detector efficiency is $\gtrsim$ 70 per cent.

3.2 The Electronics

Figure 15 is a schematic diagram of the electronics. The burst of charge collected by the detector is fed into an AAEC type 454 pulsed optical feedback preamplifier. This integrates the total charge of the pulse and converts it to a voltage signal that retains the proportionality to the energy deposited. The basic requirement for a low input capacitance to the field-effect transistor (FET) makes it necessary to d.c. couple the detector to the FET. The FET stage is allowed to build up charge equivalent to a tolerable voltage shift, at which point a light-emitting

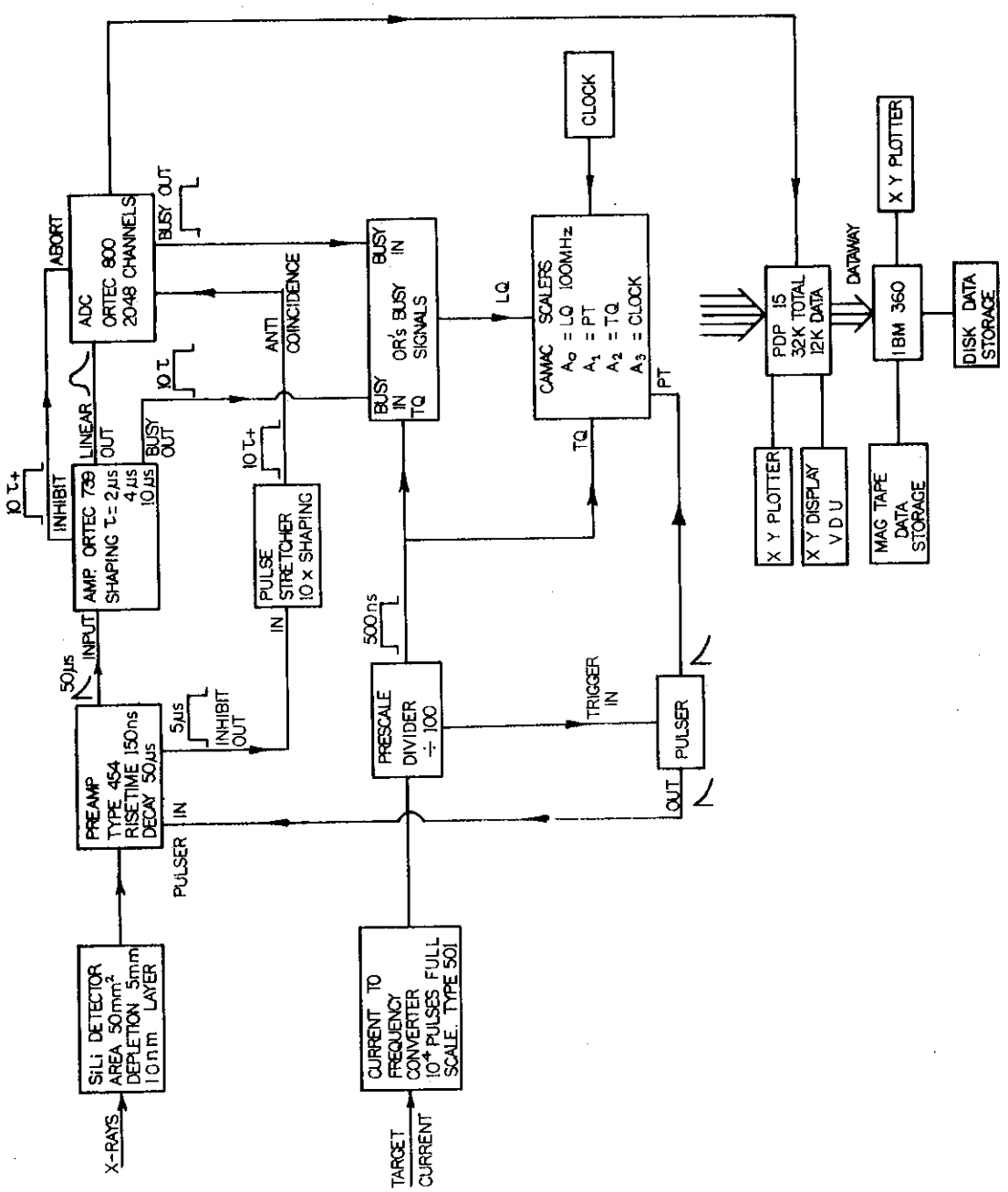

Figure 15 Electronics

diode (LED) is triggered, thus illuminating the photosensitive drain-gate FET junction which then discharges the built-up charge. This eliminates the feedback resistor which is a noisy and unreliable component. When discharge pulsing occurs, a reject waveform ('inhibit-out') is stretched and fed into the analogue-to-digital converter (ADC) anticoincidence input and all signals arriving in this time are rejected until normal operation resumes.

The linear signal from the preamplifier is sent to an ORTEC 739 amplifier where it is shaped to produce a selectable time to maximum τ = 2, 6, 10 μs and a total base width of ~ 10 τ. The amplifier has two logic outputs: a 'busy-out' of length 10 τ and an 'inhibit-out' which is also of 10 τ duration but occurs only if another pulse arrives at the amplifier within 10 τ of the first pulse. The pulse-pair resolution of the amplifier is ~ 500 ns (this includes 30 m of cable from the preamplifier to the amplifier) so any two pulses arriving within 500 ns of each other will not be discriminated against but detected as a sum of the two. Since the rise time of the preamplifier was ~ 150 ns, better pulse pair resolution (say $\lesssim$ 100 ns) could have been obtained with a small amount of extra logic. However, count rates have so far not warranted such pulse pile-up rejection systems.

It should be noted that unwanted pulses are rejected only in the ADC *via* the *ABORT IN* signal and the *ANTICOINCIDENCE* input. Since the lower level discriminator in the ADC is usually set at ~ channel 50, only pulses whose heights are situated between channels 50 to 2048, and which do not occur within 10 τ of an optical reset pulse or any other pulse, can be accepted into the spectrum.

Spectra can be analysed in real time on a PDP15 computer or sent through the AAEC Dataway system to be stored on disc or magnetic tape for more detailed analysis on a central computer.

The ADC is stabilised to keep its gain and zero (d.c. offset) constant. For most work, a ^{57}Co source (X-rays Fe Kα 6.40 keV, Kβ 7.06 keV, γ-ray 14.37 keV) has been used to set the gain at 20 eV/channel and d.c. offset to zero. The X-ray energy range is therefore 1.0 to 41 keV.

The digitised total beam charge pulses (TQ) are obtained from an AAEC type 501 current-to-frequency converter that produces 10^4 pulses per full scale deflection; the full scale range is 1 nA to 1 mA.

3.3 Typical Parameters

Beam size	40 μm to 9 mm (usually 2 mm)

Beam current	1-500 nA (depends on target damage)
Proton energy	1-3 MeV (usually 2.4 MeV)
Chamber pressure	0.5 mPa (base 0.2 mPa)
Count rates in detector	$\lesssim 10^4$ Hz (τ = 2 μs); 2000 Hz (τ = 6 μs)
Detector resolution	285 eV at 5.9 keV
Detector bias	1450 V
Amplifier gain	x 200
Shaping time constant τ	6 μs

4. PIXE SPECTRA

Typical PIXE spectra are shown in Figures 16 and 17 in which K,L,M series lines are superimposed on a background spectrum.

4.1 Background

The basic features of the observed background are as follows:

- background produced by an electrically insulated target (Figure 16);
- background from a ^{57}Co source (Figure 18);
- background from a carbon blank with and without filters (Figure 19); and
- background produced by tailing from an isolated peak (Figure 20).

The major sources of these different spectral backgrounds are:

(i) Bremsstrahlung due to secondary electrons.

(ii) Bremsstrahlung due to projectile acceleration in the matrix.

(iii) Compton scattering of high energy X-rays and γ-rays produced from nuclear excited states.

(iv) Bremsstrahlung produced by accelerated electrons near a charged insulated target.

(v) Low energy tailing.

Other authors have discussed backgrounds produced by thin and thick targets [Johansson *et al.* 1970, Flochini *et al.* 1972, Kaji & Shiokawa 1977].

4.1.1 Secondary electron bremsstrahlung

For PIXE spectra, the bulk of the background produced in the 0-10 keV X-ray energy region is caused by secondary electron bremsstrahlung (Figure 19). An incident particle (proton) of energy E_p ejects an electron of energy E_e at point A (Figure 21) in the direction θ_e in the target and the electron then loses its energy, its value being E_e' at

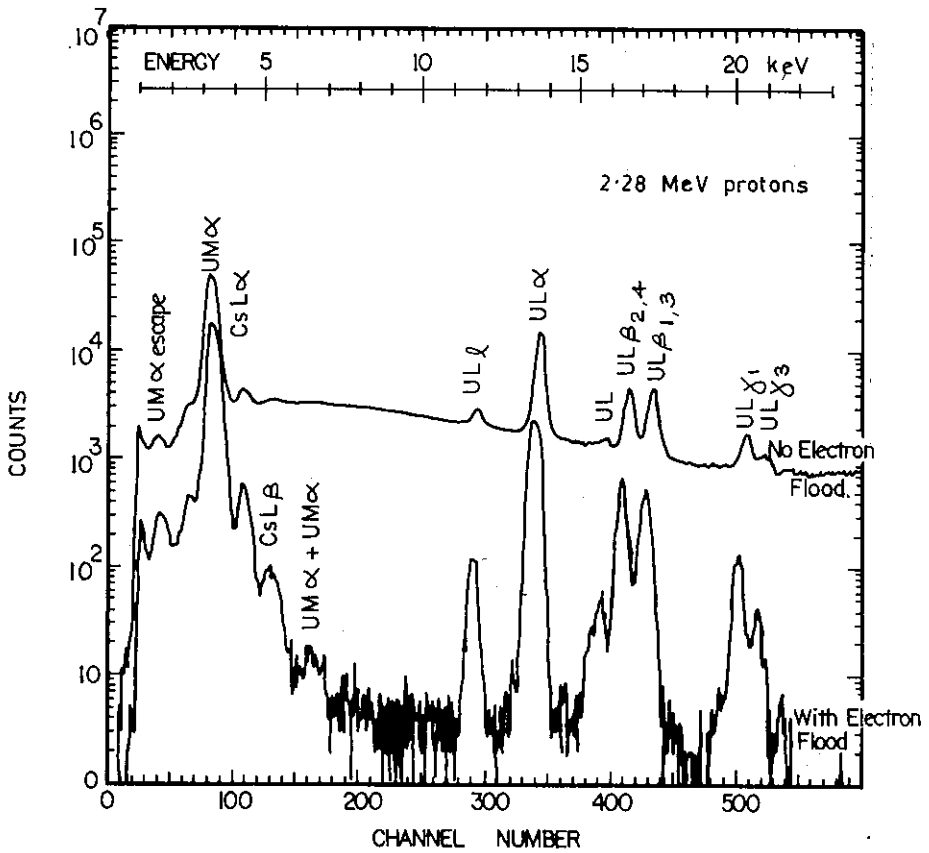

Figure 16 UO_2 L and M X-rays Including Use of Electron Flood

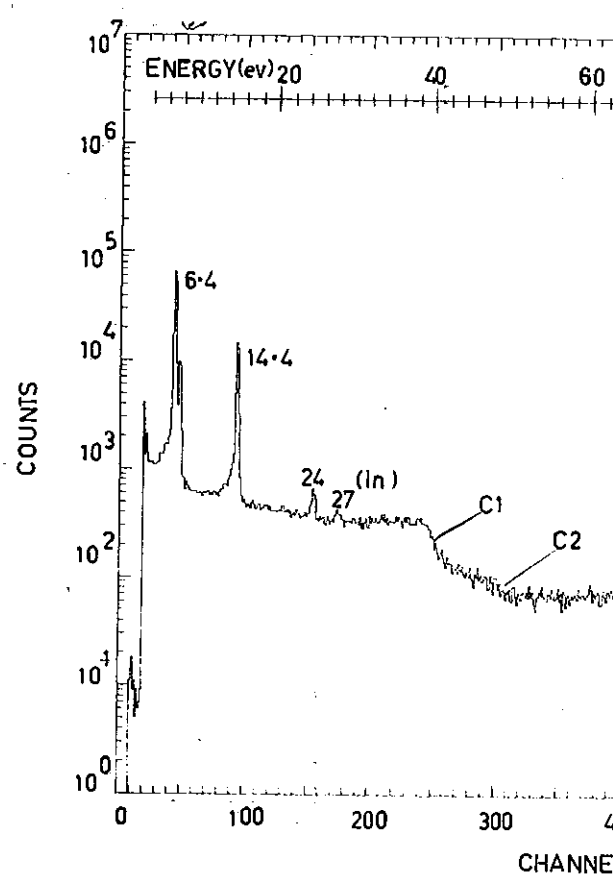

Figure 18 X-ray

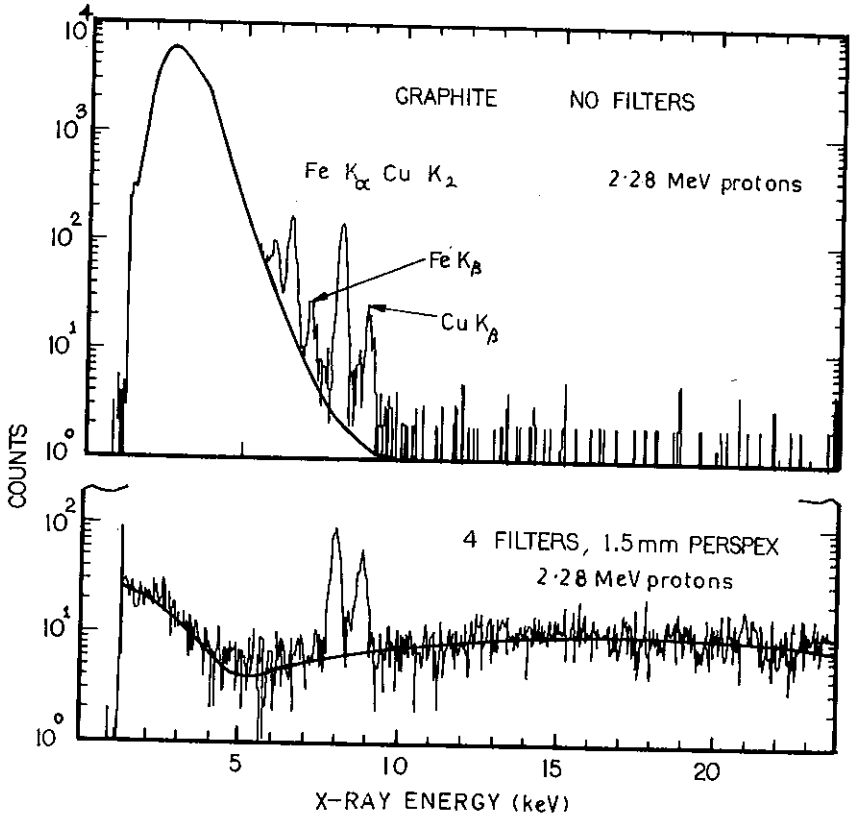

Figure 19 Background Radiation from a Carbon Matrix With/Without Filters

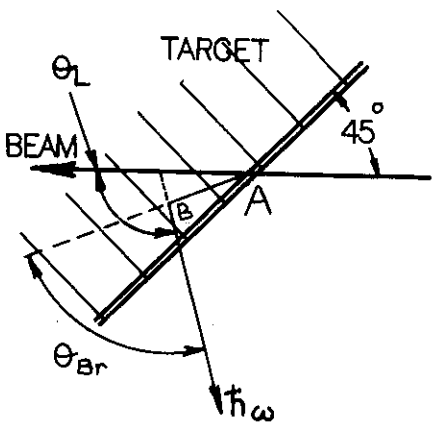

SCHEMATIC DIAGRAM OF THE ORIGIN OF BREMSSTRAHLUNG BY SECONDARY ELECTRONS

Figure 21 Bremsstr

point B where it produces bremsstrahlung of energy $E_x = \hbar\omega$ in direction θ_B. These electrons come from strongly bound orbits K,L,M where, before impact, they already had high velocities. The maximum bremsstrahlung energy E_{max} (keV) that an incident proton of energy E_p (MeV) can transfer to an electron at rest in a free collision is

$$E_{max} = \frac{4\, m_p m_e E_p}{(m_p+m_e)^2} = 2.18\, E_p \text{ (keV)} \quad ; \qquad (14)$$

in the present case for $E_p \sim 2.3$ MeV, E_{max} is ~ 5.0 keV. From the carbon blank results (Figure 19), it would appear that the secondary electron bremsstrahlung is more than 1 in 10^3 less than its maximum value at an energy equivalent to 1.5 E_{max}. For energies greater than E_{max}, Folkmann *et al.* [1974a] have suggested that the differential cross section for the production of secondary electrons decreases as $\sim E_x^{-10}$.

The angular dependence of bremsstrahlung from secondary electrons is shown in Figure 21 for E_{max} = 3 and 9 keV with intensities normalised at $\theta = 90°$. The intensity of the spectrum at $\sim E_{max}$ reaches a maximum at $\theta_L = 90°$ and then becomes less in the forward and backward directions. Kaji & Shiokawa [1977] suggest that there will be a 50 per cent reduction in the background if the 135° (backward) angle is used instead of the 90° angle. This reduction in background will obviously also be reflected as an increase in the detection limits of trace elements whose characteristic X-ray lines fall in the region of, say, 0 to 2 E_{max}.

In addition to the ejected electrons arising from direct impact of protons on the atom, there will be, especially for light matrix atoms, many Auger electrons. The energy of these electrons will be generally much less than E_{max}, so they are unimportant to the production of background radiation.

4.1.2 Proton bremsstrahlung

Proton bremsstrahlung is produced by large accelerations which occur during close collisions between the projectile and the nuclei of the matrix. The cross section for this process decreases with the projectile energy in contrast to the secondary electron case which increases rapidly as $\sim E^4$.

Folkmann *et al.* [1974a] point out that the cross section for projectile bremsstrahlung contains a term $[(Z/A)_{projectile} - (Z/A)_{matrix}]^2$ arising from interference between the radiation of the projectile and that of the recoiling nucleus. The projectile bremsstrahlung can therefore

be made to vanish if the charge-to-mass ratios for the matrix nuclei and the projectiles are the same. This is not the case for proton bombardment where $(Z/A)_{proton} = 1$ and $(Z/A)_{matrix}$ is $\sim 1/2$.

For α particles and heavy ions with $(Z/A) \sim 1/2$, the projectile bremsstrahlung can in principle be disregarded but, in practice, there is a comparable or even larger contribution to the background from Compton scattering of nuclear de-excitation γ-rays [Watson *et al.* 1975].

In contrast to the two-step electron bremsstrahlung, the angular distribution of the projectile bremsstrahlung reaches a minimum at 90°. However, the deviation from isotropy is generally so small (15-20 per cent) that it is insignificant.

In summary, there is not much that can be done to reduce the bremsstrahlung background. At best, the angular distributions vary by $\sim$ 50 per cent for secondary electron bremsstrahlung but only by 20 per cent for projectile bremsstrahlung — maximising at 90° for secondary electron bremsstrahlung and minimising at 90° for projectile bremsstrahlung. This suggests that the angle of the detector must be chosen to suit a particular X-ray energy E_x. For $E_x \gtrsim (2\ E_{max} = 10\ keV)$, the 135° backward angle would be the best to reduce the secondary electron bremsstrahlung, whereas the 90° angle would be best for $E_x \lesssim (2\ E_{max})$; however E_{max} is also a function of the projectile energy since $E_{max} = 2.18\ E_p$.

Note also that the sample thickness, which would allow the secondary electron to escape from the matrix before emitting bremsstrahlung radiation, is too small (*i.e.* $\lesssim$ 50 μm for carbon).

4.1.3 Compton scattering

The proton beam will excite nuclear levels which, through their decay, will give rise to γ-radiation. Compton scattering, which converts the γ-rays to a continuous background in the X-ray region, depends on the material of the detector and its near surroundings. This background is often larger than the background produced by proton bremsstrahlung. The authors have observed this to be between 10 and 50 times higher than the proton bremsstrahlung.

The background is strongly dependent on concentrations in the matrix of special elements with high cross sections for excitation of low-energy nuclear levels, such as ^{19}F and ^{23}Na. The importance of the γ-ray background has been discussed by Folkmann *et al.* [1974b]. Since

it is dominant for $Z > 30$ at E_p = 3-5 MeV, the bombarding energy must be as low as possible for minimum γ-ray background, yet still able to give a reasonably large X-ray yield.

This proton energy E_p must be below the threshold for inelastic scattering of the most abundant nuclides in the matrix, usually ^{12}C and ^{16}O. Projectile energies of 1-3 MeV atomic mass unit (amu) are the best choice.

Heavy ions have a higher energy, and consequently a higher cross section, for γ-ray production than protons of the same velocity. According to Johansson & Johansson [1976], this is a great disadvantage which might offset the gain from a Z^2 term in the cross section for characteristic X-ray production. For this reason, protons are generally used.

Kaufmann & Akselsson [1977] have discussed Compton scattered electrons in or near the detector, originating from high energy X- and γ-rays. The sample thickness and composition, and the amount of absorbing material between the sample and the detector can alter the relative contribution of the Compton electron component. The secondary electron bremsstrahlung will be attenuated by any absorptive material present (*e.g.* filters) but the Compton electron component will not; however, it is felt that this contribution is small because of the small range of electrons in the detector.

Two types of Compton scattering are relevant to this discussion:

(i) High energy X-rays and γ-rays produced upstream of the target (*e.g.* at the aperture, *etc.*) are Compton scattered through 90° in the *target* and end up in the detector.

(ii) High energy X-rays and γ-rays produced by nuclear reactions in the target are Compton scattered in the *detector* and the energy deposited is detected as background.

Standard theory gives

$$\Delta = E_0 - E' = E_0 \left[\frac{\alpha}{1+\alpha}\right] \quad , \qquad (15)$$

where $\alpha = \frac{E_0}{mc^2} (1-\cos\theta)$,

mc^2 = 0.511 MeV,

E_0 = initial photon energy,

E' = scattered photon energy, and

θ = scattering angle .

Δ is obviously a maximum when $\theta = 180°$ for backscattered photons, and

TABLE 4

TYPICAL NUCLEAR REACTIONS

THAT PRODUCE GAMMA-RAYS

Reaction	γ-ray Energy
$^{19}F(p,p'\gamma)\ ^{19}F$	0.110 (MeV)
$^{56}Fe(p,\gamma)\ ^{57}Co$	0.128
$^{27}Al(p,p'\gamma)\ ^{27}Al$	0.178
$^{19}F(p,p'\gamma)\ ^{19}F$	0.197
$^{23}Na(p,p'\gamma)\ ^{23}Na$	0.439
$^{16}O(p,\gamma)\ ^{17}F$	0.496
$^{14}N(p,\gamma)\ ^{15}O$	0.75
$^{35}Cl(p,\gamma)\ ^{36}Ar$	0.797
$^{32}S(p,\gamma)\ ^{33}Cl$	0.806
$^{27}Al(p,p'\gamma)\ ^{27}Al$	1.013
$^{23}Na(p,\gamma)\ ^{24}Mg$	1.368
$^{28}Si(p,\gamma)\ ^{29}P$	1.384
$^{24}Mg(p,\gamma)\ ^{25}Al$	1.54
$^{12}C(p,\gamma)\ ^{13}N$	2.366
$^{31}P(p,\gamma)\ ^{32}S$	2.44

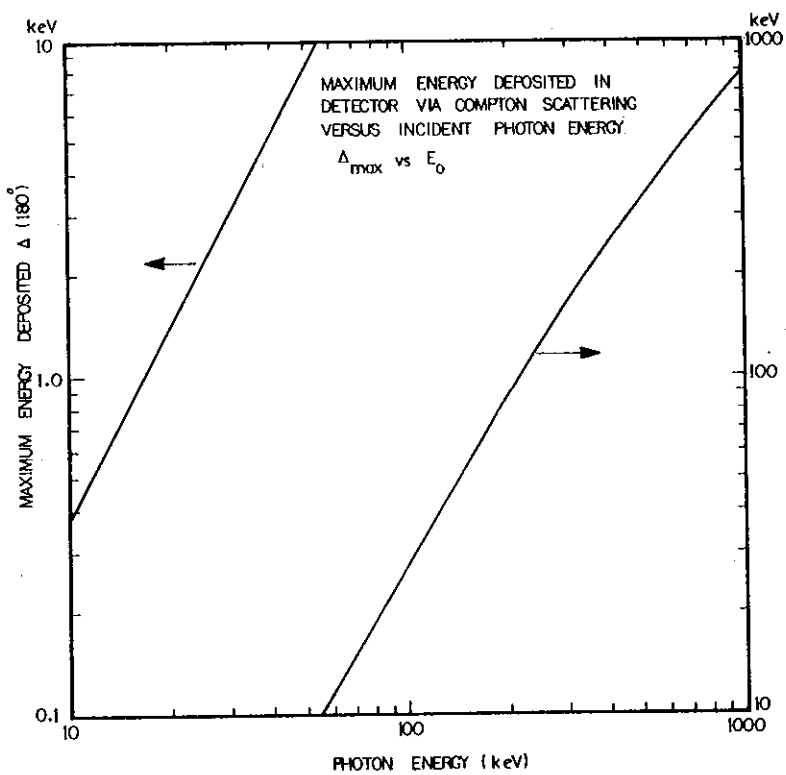

Figure 22 Maximum Energy Deposited in Detector *via* Compton Scattering

ranges from 0 to Δ_{max} as the scattered angle varies from 0 to 180°, thus giving rise to the well-known Compton edge.

The authors have certainly seen this effect for case (i). The 2 mm aperture, which is made of brass (Cu-Zn), is sited ~ 2 m upstream from the target. Protons impinging on this produce not only γ-rays but also Cu and Zn X-rays which travel down to the target, Compton scatter through 90° and are then detected in the detector. Substitution in Equation (15) for Cu Kα (E_0 = 8 keV) gives Δ (90°) = 123 eV. This energy will remain in the target and an X-ray of energy $E_0 - \Delta$ = 7.88 keV will be detected; this represents a very small shift from the expected 8 keV.

The cross section for inelastic scattering does, however, show a characteristic minimum (about 50 per cent lower than the forward or backward directions) at about 90-100°. This favours the 90° geometry for Compton scattering in the *target* reaching the detector.

For case (ii), Compton scattering of high energy X-rays or γ-rays actually occurs in the detector. Assuming that the γ-rays escape or pass right through the detector after scattering, the residual energy in the detector that will contribute to the background can be calculated. Figure 22 shows a plot of Δ (180°) versus E_0. For the X-rays considered, $E_0 \lesssim 30$ keV, less than 3 keV is deposited in the detector, and will appear in the secondary electron bremsstrahlung region. This background consideration is of primary importance in the 10-30 keV region and for all photon energies greater than 50 keV. Typical nuclear reactions that produce γ-rays are given in Table 4.

All γ-ray energies are typically >> 50 keV, so it is not even necessary to go to the extreme case of backscattering (θ = 180°) to deposit energies between, say, 10 and 30 keV in the detector.

Figure 18 shows the γ-ray spectrum from the ^{57}Co source. The step increase in background due to the Compton edges C_1 to C_4 is clearly seen, as are the C_1 and C_2 edges produced by the 122 and 136 keV γ-rays coming from the ^{57}Co source. All of these edges increase the background in the 0-30 keV X-ray region.

In summary, it can be said that the 90° geometry used at present will minimise the background contributions from high energy X-rays and γ-rays which Compton scatter in the target and then reach the detector. It is more difficult, however, to reduce the background component produced by Compton scattering of γ-rays in the detector. These two background

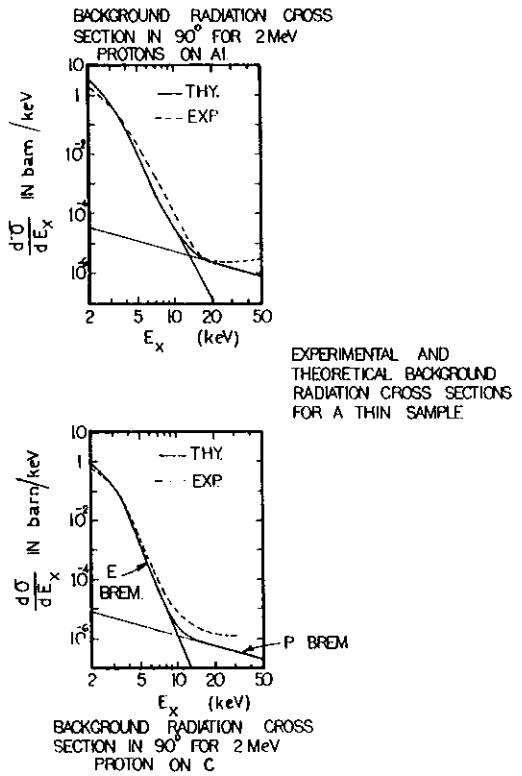

Figure 23 Experimental and Theoretical Background Radiation for Thin Sample C and Al

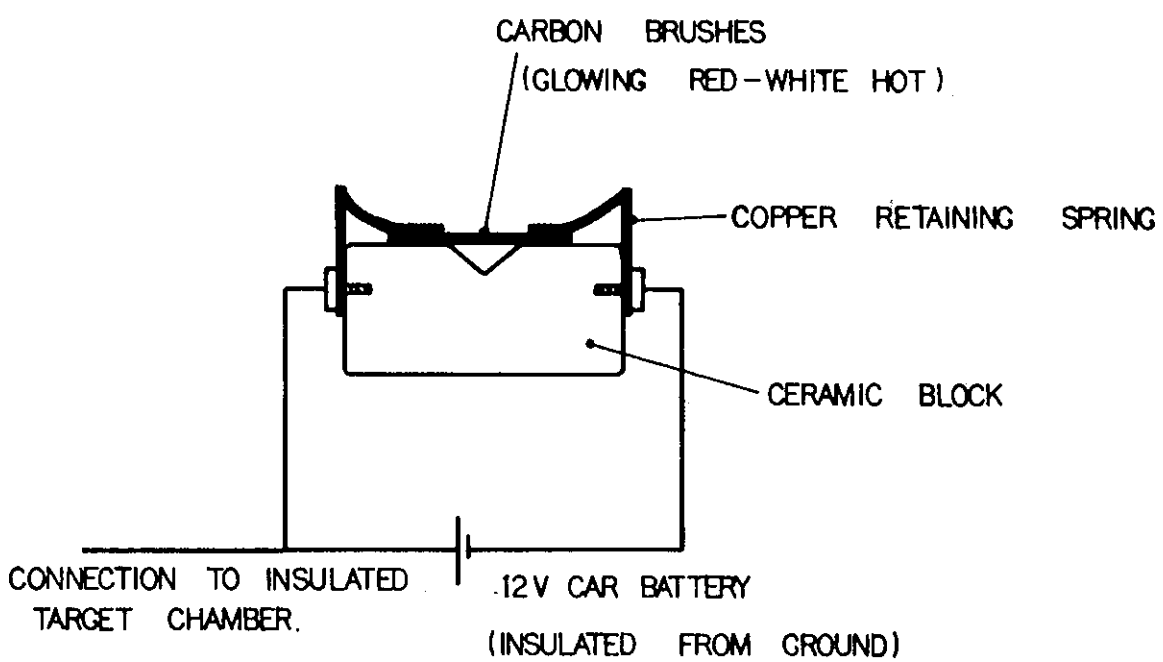

Figure 24 Equipment for Electron Flood

components will be the major contributions to background in the X-ray energy region $E_x \gtrsim 2\ E_{max}$ and hence are the factors limiting the ultimate PIXE sensitivity in this region.

Figure 23 [after Folkmann *et al.* 1974a] shows experimental and theoretical background for aluminium and carbon matrices. The increased backgrounds in the $\gtrsim$ 10 keV regions are due to the Compton scattering of the resultant γ-rays.

4.1.4 Target charging

Samples with poor electrical conductivity may be charged (during bombardment), theoretically to the voltage of the incident protons 2 MV. The target can thus attain high potentials which will accelerate any free electrons nearby, producing large amounts of bremsstrahlung radiation at energies much higher than the E_{max} discussed previously (see Figure 16). To overcome this problem, the target is sprayed with electrons from a hot carbon filament [see Ahlberg *et al.* 1975]. Figure 24 shows the carbon filament and battery device used at the AAECRE. As an alternative, the chamber pressure can be slightly raised to overcome charging, but this reduces the low energy X-ray yield.

4.1.5 Low energy tailing

A single X-ray energy peak in a spectrum is commonly represented by a Gaussian distribution which reflects the statistical nature of the system noise and the charge collection process. In practice, an isolated peak generates an almost linear contribution to the background at energies much lower and higher than the peak energy plus a low energy exponential tail closer to the peak. These so-called 'steps' and 'tails' are attributed to incomplete collection of ionisation charge and to electron escape from the sensitive detector region. The count rates in the tail of any peak are typically about 300 to 1200 times less than the peak value.

Tailing can be suppressed by shielding the edge region of the detector with smaller aperture windows (the authors are already using a guard ring detector). Bragg spectrometry (wavelength dispersive techniques) avoids this problem; it does not, however, have the capability of simultaneously measuring several elements.

The incomplete charge collection is attributed to a dead layer at the entrance face of the detector. The reason for this dead layer seems to be that some of the electrons which are formed at the photon interaction point diffuse into the surface (where they are lost) before their

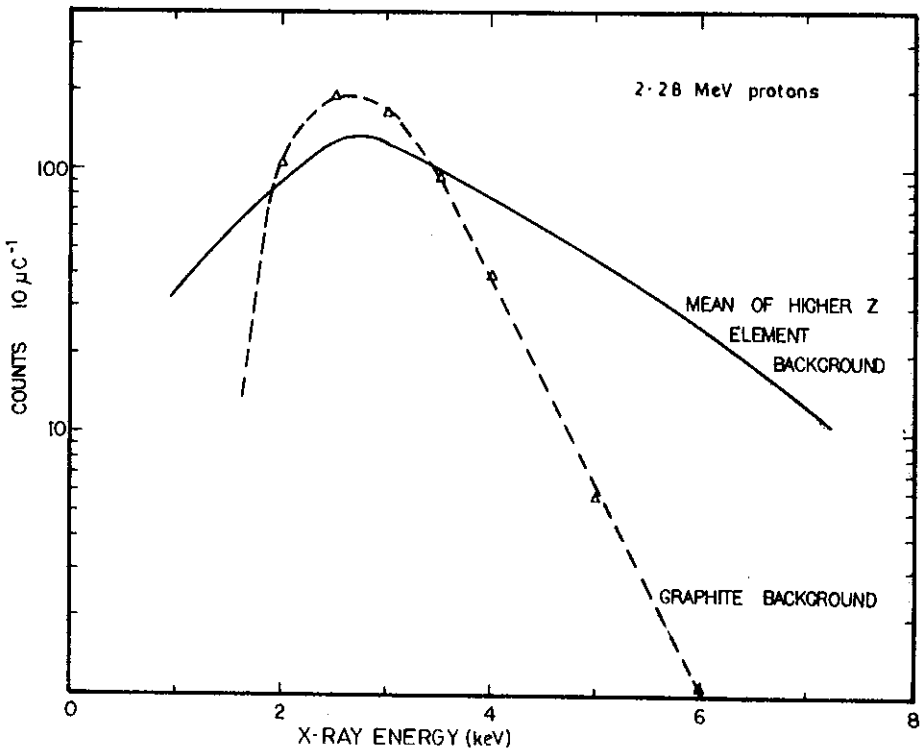

Figure 25 Experimental Background from Carbon or Higher Z Elements

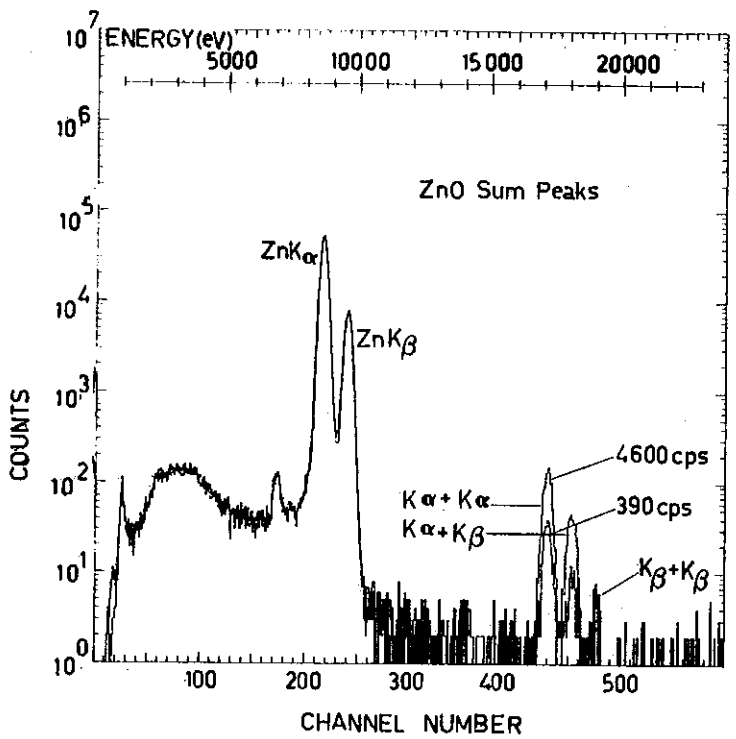

Figure 26 Pile Up in ZnO Spectrum

motion in the collecting electric fields removes them from the region of the surface. Goulding [1977] assumes that electrons are lost if their diffusion distance exceeds their drift distance; he has produced the following expression for dead layer thickness:

$$d = \frac{RT}{q} \frac{\mu}{v_s} \qquad (16)$$

where T = temperature (K),

q = electronic charge,

μ = electron mobility, and

v_s = terminal velocity of electron in the electric field.

For Si at 77 K, $\mu \sim 4 \times 10^4$ cm^2 v_s^{-1}

$v_s = 10^7$ cm s^{-1}

$\therefore \quad d = 0.28$ μm.

This rather thick dead layer (~ 0.3 μm) is produced by basic physical processes and represents a fundamental limit rather than being a consequence of manufacturing processes. Figure 20 shows this effect for an isolated peak; the low energy tail of the peak and the increased background for all energies below the peak (the step) are clearly seen.

Figure 25 shows the general experimental background shapes in the energy region 2 to 8 keV for a light matrix, *e.g.* carbon, and a mean of several heavier matrices. The increased γ-ray component of the background is clearly seen in the 4 to 8 keV region.

In summary, Folkmann *et al.* [1974a] have said "PIXE gives lower levels for continuous background radiation than X-ray tubes or γ-ray sources and hence a better sensitivity".

4.2 Peaks

Three types of peak superimposed on the background continuum have been observed:

(i) Discrete K, L and M characteristic X-ray peaks. The production of these has been already discussed. The areas under these peaks are directly related to the elemental concentration.

(ii) Sum peaks produced by electronic pileup.

(iii) Escape peaks produced in the detector.

4.2.1 Sum peaks

Pileup into a sum peak occurs if a second pulse enters the amplifier at a time after the detection of the first photon that is less

than the pulse-pair resolution time of the amplifier; this is subsequently referred to as the amplifier blind time. Figure 26 shows the effects of summing peaks for high and low count rates into the spectrum; the sum peaks for (Kα+Kα), (Kα+Kβ) and (Kβ+Kβ) are clearly distinguished. If the pulse separation time is greater than this blind time, then both pulses will be recognised, and if the separation time is less than ten times the pulse shaping time of the amplifier, an inhibit signal will be produced which is fed to the abort input of the ADC.

The blind time of the amplifier was directly measured using two pulsers fed to the test input of the preamplifier. One of the pulsers was triggered by the other, the delay time between them being adjustable. The blind time was the measured delay time between the pulses when sum peaks in the spectrum were no longer detected. Measurements of blind time were made with pulses of various heights (*i.e.* energies). The blind time was shown to be a function of energy (Figure 27) and fitted to the relationship:

$$\tau(E) = (540 + 21\ E)\ \text{ns} \quad . \tag{17}$$

If a pulse with energy E_1 is accepted for measurement and an E_2 pulse arrives within the blind period τ_{12}, then a count in the sum energy $E_1 + E_2$ position will be registered. To first order approximation, the pile will be registered. To first order approximation, the pileup into the sum peak will be

$$\frac{A_1}{T_L} \cdot \tau_{12} \cdot A_2 \quad ,$$

where A_1 and A_2 are the counts registered in the respective E_1 and E_2 positions and T_L is the total live time. There will be a similar probability of the E_1 pulse following the E_2 pulse. The total counts registered for the live time in the sum peak will therefore be

$$A_S = \frac{A_1 A_2}{T_L} (\tau_{12} + \tau_{21}) \quad . \tag{18}$$

If $E_1 = E_2$, *i.e.* the peak summing with itself,

$$A_S = \frac{A_1^2}{T_L} \tau_{11} \quad . \tag{19}$$

Statham [1977] gives a rigorous treatment of the mathematical analysis of pileup effects and lists his own measurements of the blind time together with those made by Charnley [1977] and Kandiah [1973]. He suggests that sum peak production should be measured for particular peak combinations that are going to be troublesome in later analysis.

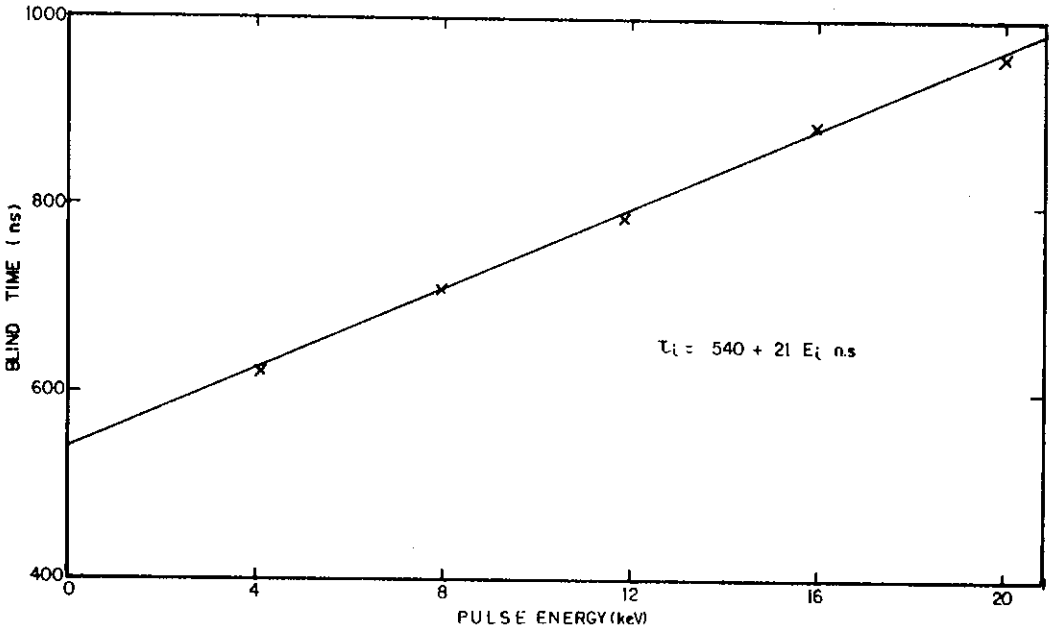

Figure 27 Blind Time of Amplifier

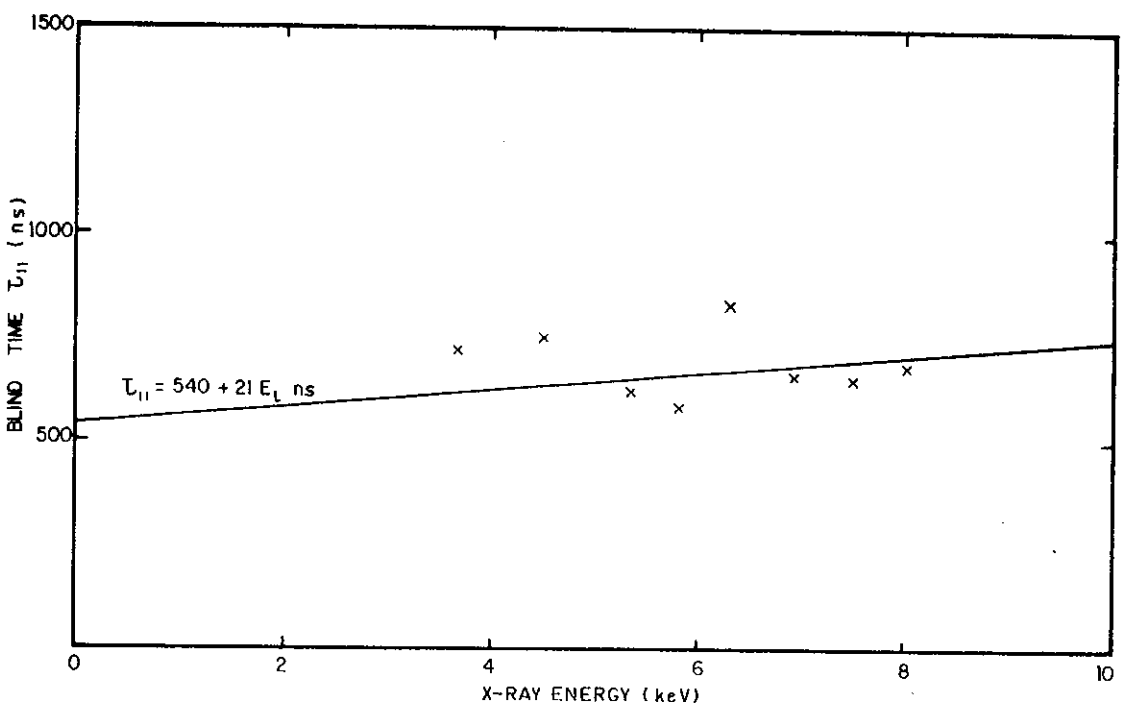

Figure 28 Blind Period (τ_{11}) for Sum Peaks into Channel Ex + Ex

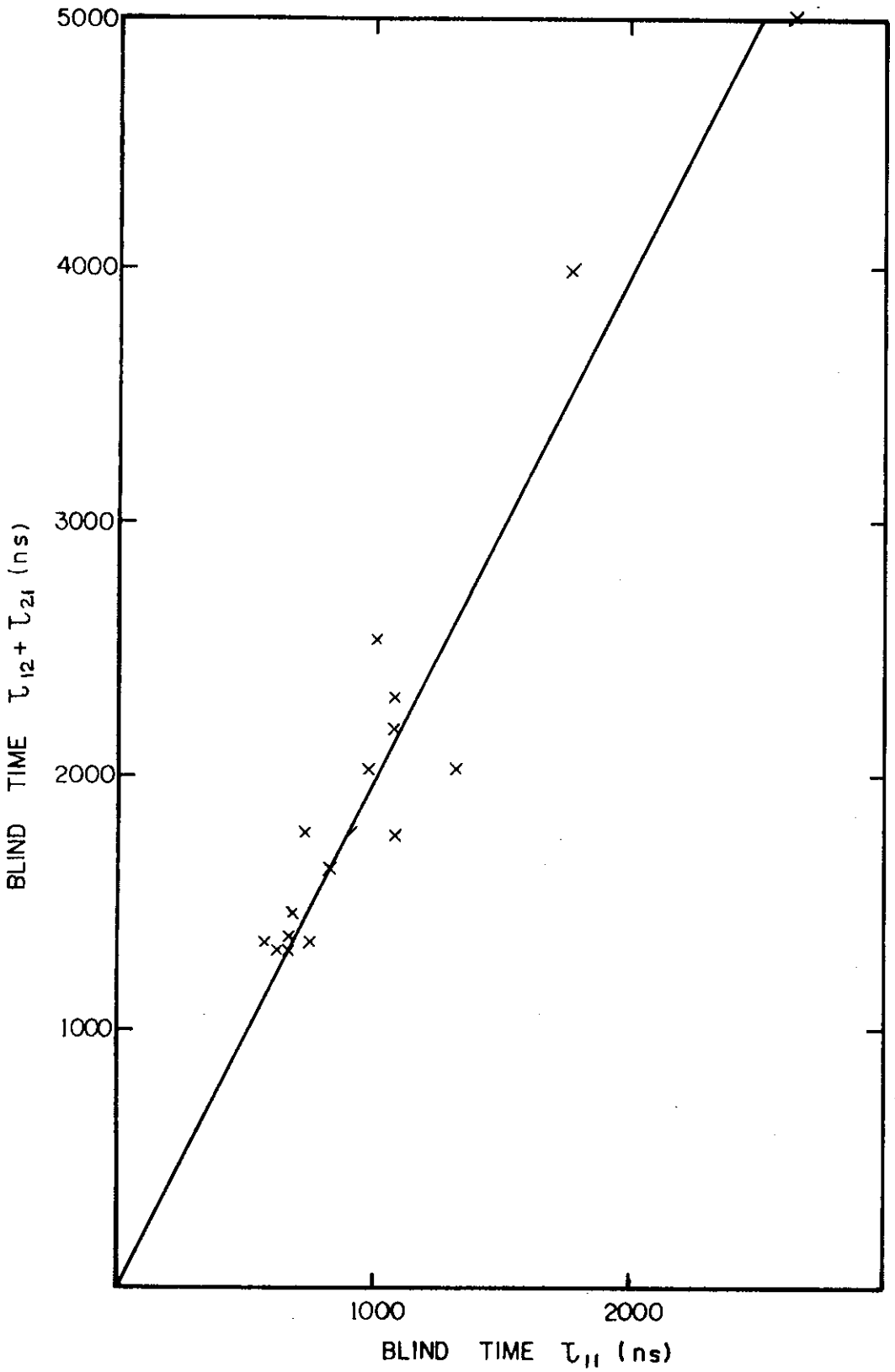

Figure 29 Sum Peak in Channel $E_1 + E_1$ *versus* Sum Peak in Channel $E_1 + E_2$

We have found, however, that this blind period can not only be predicted but is, in fact, directly related to the measured amplifier blind time. The blind time τ_{11} was measured from a number of spectra and plotted against E_1 (Figure 28). It can be seen that the τ_{11} data have a good fit to the previously measured blind time $\tau(E)$ (Equation (17)).

Pileup into the E_1 and E_2 channels has been plotted against pileup into the E_1+E_2 channel. (In all cases, A_1 is about seven times greater than A_2 so the weighted energy is similar to E_1 (see Figure 29).)

From the gradient of this plot, it can be seen that

$$(\tau_{12}+\tau_{21}) \approx 2\ \tau_{11} \quad . \tag{20}$$

Pileup into the E_1+E_2 channel can therefore be estimated for all energies. A count weighted energy should be used for the calculation of τ_{11}.

To correct completely for sum pileup, it would be necessary, at each E_i in the spectrum containing A_i counts and at each energy E_j containing A_j counts, to compute $A_iA_j\tau_{ij}/T_L$. This would be subtracted from channel E_i+E_j and then be added back to E_i.

The correction to the count in E_i will be negligible but the sum count at E_i+E_j should be calculated and removed from the spectrum before final analysis to avoid confusion with a trace element X-ray peak at this energy.

4.2.2 Escape peaks

There is a finite probability that an X-ray of energy E_x in the detector will interact with a silicon atom in the detector, thus producing a silicon X-ray which will then completely escape from the detector. The energy deposited in the detector is then $(E_x - 1.74)$ keV. These events are lost from the full energy peak and reappear in the spectrum as a separate peak of energy (E - 1.74) keV. Figure 30 shows typical escape peaks produced by Ni K X-rays. The escape probability increases with decreasing incident X-ray energy down to the K absorption edge of silicon. This is to be expected since the lower energies are deposited nearer the detector surface and so have a greater chance of completely escaping. Figure 31 shows our measured probabilities together with the theoretical ones of Woldseth [1975].

5. FILTERS

Material placed between the target and the detector will exponentially

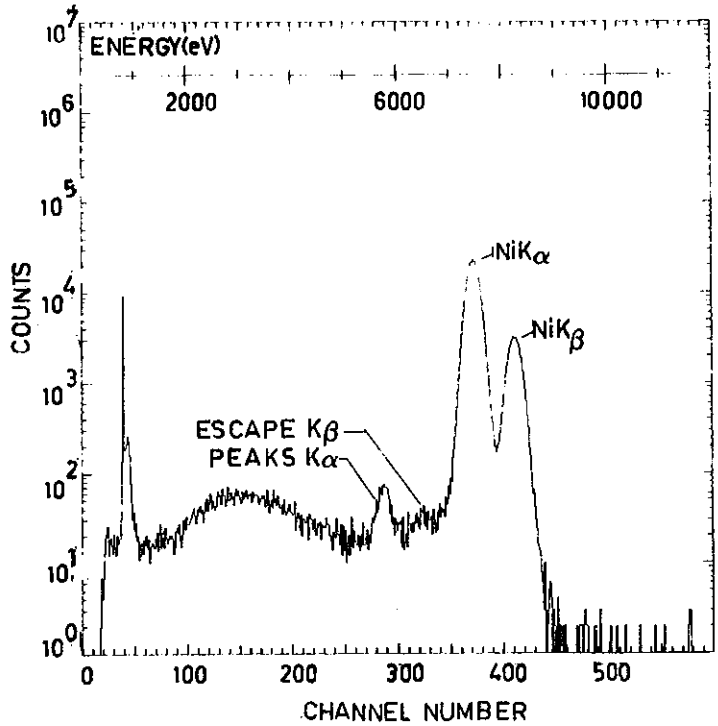

Figure 30 Escape Peaks in NiO_2 Spectrum

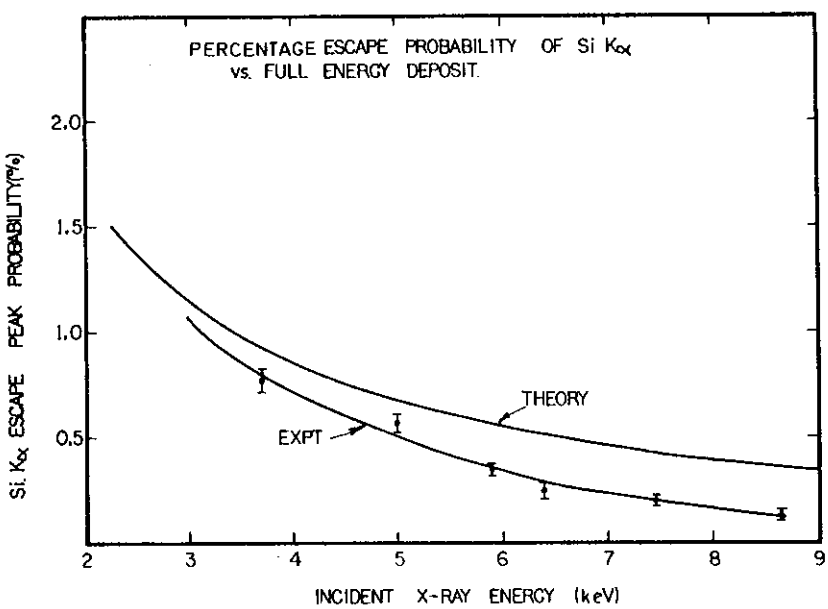

Figure 31 Production of Escape Peaks Experiment Theory Data

attenuate the number of X-rays reaching the detector:

$$N = N_0 \exp[-\mu x\rho] \quad , \tag{21}$$

where N_0 = initial number of X-rays, and

N = number of X-rays at depth x in material with mass absorption coefficient μ and density ρ.

The energy dependence of μ follows roughly the form E^{-3} between absorption edges, but sharp discontinuities in μ occur at K,L,M..... absorption edges. In Figure 5, μ versus E is plotted for various matrix elements. At low Z, the exponent of E increases to about -3.5; for a given energy, μ varies approximately as Z^4.

Layers of 1.5 mm thick Perspex placed on top of the detector have been used. The value of μ for Perspex was not known, but for the present work the following reasonable assumption was made:

$$\mu \propto Z^4/E^3 \quad . \tag{22}$$

Combining Equations (21) and (22)

$$\text{Eff \%} = \frac{N}{N_0} 100$$

$$= 100 \exp\left[-\frac{AT}{E_x^3}\right] \tag{23}$$

where Eff % = percentage efficiency,

A = constant for a fixed Z (Perspex),

T = number of layers of Perspex 1,2,....5, and

E_x = energy (keV) of X-ray line of interest.

The percentage efficiencies at seven different X-ray energies E_x were measured for four different filter layers (T = 1,2,3,5) and a mean value of the constant A was calculated for the 28 readings:

$$A = 588 \pm 45 \ (8\%) \quad .$$

No trends were seen in the dependence of A on energy or filter thickness. Hence, Equation (23) becomes

$$\text{Eff \%} = 100 \exp[-588\ T/E^3] \quad , \tag{24}$$

which is valid for 4 keV < E < 20 keV

$$T = 1,2,...5 \text{ layers of 1.5 mm thick.}$$

From Equation (24), an equivalent T can be derived for the T = 0 case. Although T = 0 is the no filter case, there are still two 25 μm beryllium windows separated by a 3 cm air gap and approximately 50 $\mu g\ cm^{-2}$ of gold interposed between the target and the detector. Their equivalent

transmission with energy is shown in Table 5.

TABLE 5

FRACTIONAL TRANSMISSION WITH ENERGY

X-ray Energy (keV)		1.55	1.77	2.07	2.48	3.10	4.13	4.96	6.20	8.27
Element	Thickness	Transmission								
Au	10 nm	0.96	0.97	0.97	0.97	0.97	0.98	0.98	0.99	1.00
Air	3 cm	0.021	0.070	0.19	0.37	0.60	0.80	0.88	0.94	0.97
Be	50 μm	0.20	0.34	0.50	0.67	0.81	0.91	0.94	0.97	0.99
Total Eff.%		0.4	2.3	9.0	24.0	47.0	71.0	81.0	90.0	96.0
Equivalent T		0.035	0.036	0.036	0.037	0.038	0.041	0.044	0.043	0.039

Fitting the total Eff % of Table 5 to Equation (24), the zero filter case T = 0 has an equivalent T = 0.039 ± 0.004 layers of 1.5 mm thick Perspex, that is

$$\text{Eff \%} = 100 \exp[-(23 \pm 4)/E^3] \qquad (25)$$

for the zero filter case. Since Perspex has a low Z, it might have been better to fit $E^{-3.5}$ dependence instead of E^{-3}. However, quite acceptable values can be obtained using Equation (25). Figure 14 shows a plot of detector efficiency (Eff %) versus X-ray energy for various layers of Perspex.

As the energy increases, the probability of X-rays going right through the 5 mm detector increases and the detector efficiency decreases, with the form

$$\text{Eff \%} = 100\left(1-e^{-\mu_{Si}}\right)^{x\rho} , \qquad (26)$$

where μ_{Si} = mass absorption coefficient of Si ,

x = depletion thickness ~ 5 mm, and

ρ = density of Si, 2.329 g cm^{-3} .

The detector has 100 per cent efficiency for X-ray energies less than 20 keV, but this drops to ~ 2 per cent at 100 keV. From Figure 14 it can be seen that

$$\text{Eff \%} > 50\% \quad \text{if} \quad 3 < E < 40 \text{ keV}$$

$$\text{Eff \%} > 90\% \quad \text{if} \quad 10 < E < 20 \text{ keV}.$$

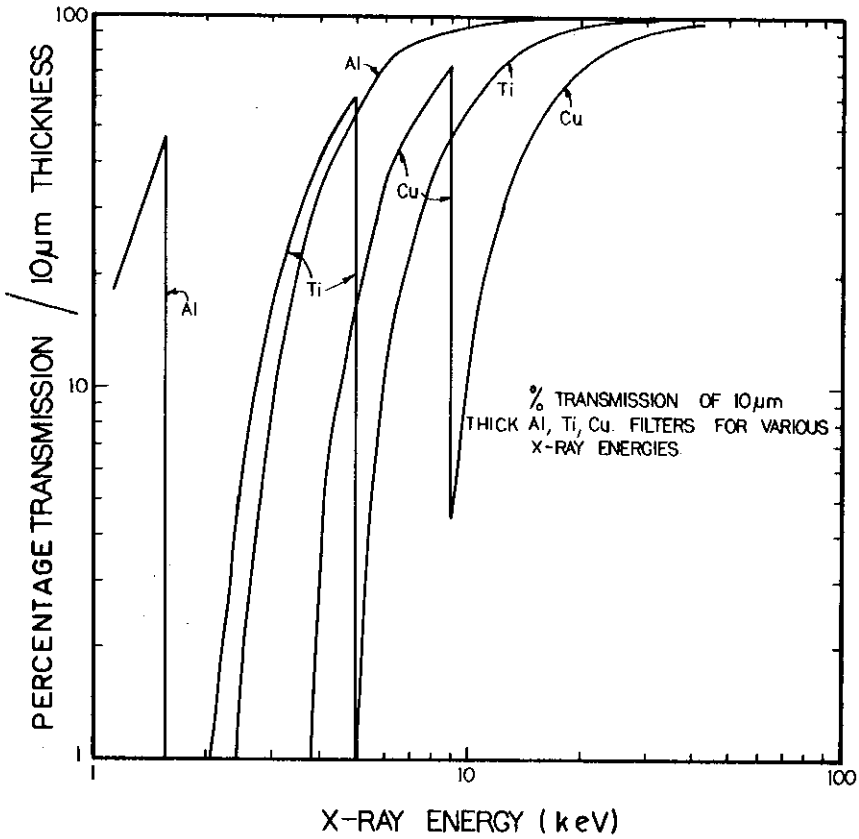

Figure 32 % Transmission *versus* Energy for Various Filters (10 μm thick)

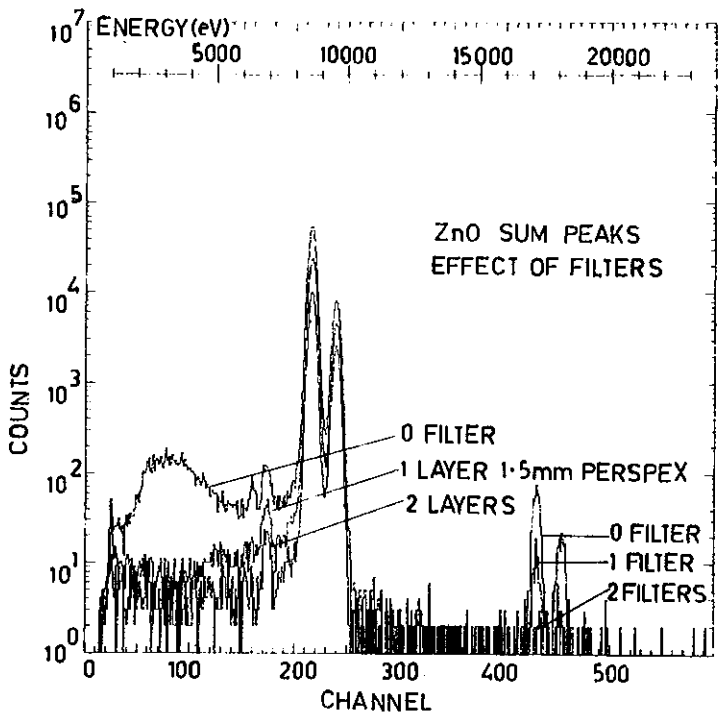

Figure 33 Use of Filter to Reduce Sum Peaks

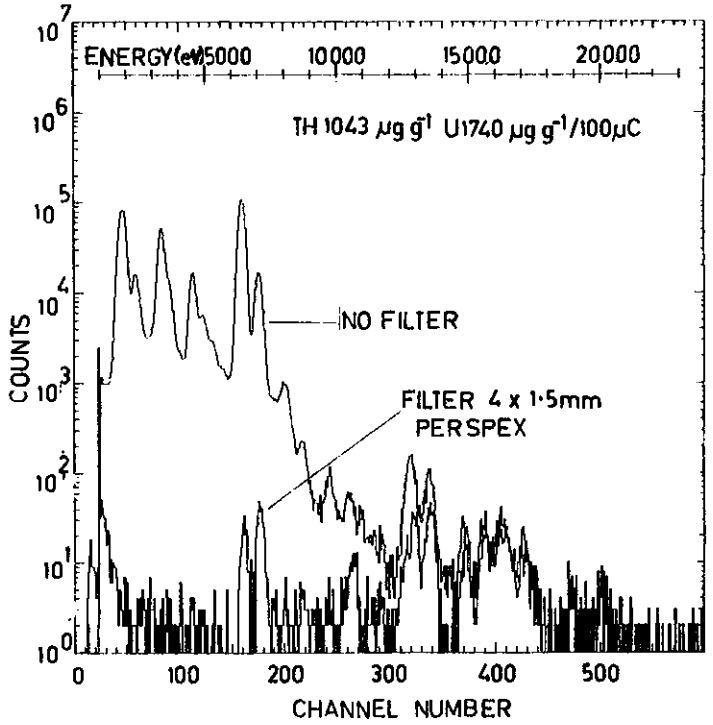

Figure 34 Use of Filter for Enhancement of High Energy X-rays

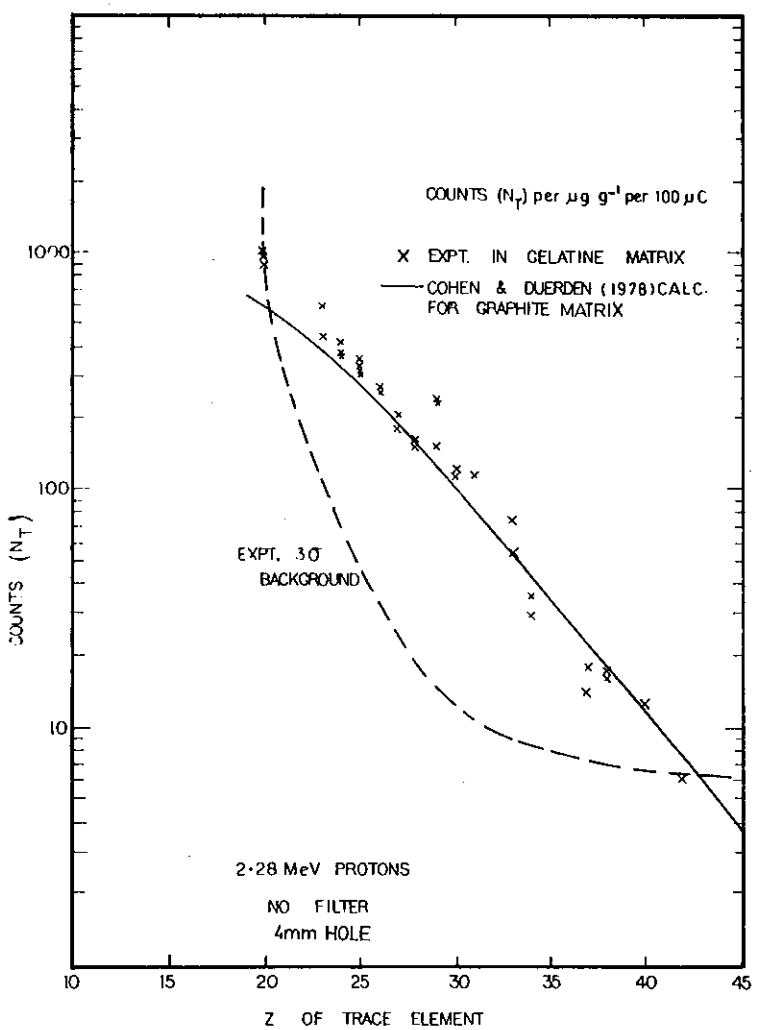

Figure 35 Counts Under Peak/μg g^{-1}/100 μC *versus* Z

Perspex is a hydrocarbon and as such has its K absorption edges < 1 keV. The sharp discontinuities that occur at the K,L,M edges are not a problem and the layers of Perspex effectively become a high-pass filter whose 3 dB point with energy is determined only by the number of layers of Perspex used.

Other materials of higher Z can be used as filters. The percentage transmissions for 10 μm thick Al, Ti, and Cu are shown in Figure 32. As can be seen, there is a sharp rise in transmission just below the K absorption edge, making these types of filter very useful as band-pass filters for energies $E_x < E_{Kabs}$ and high-pass filters for energies $E_x > E_{Kabs}$. The main problem with filters of higher Z values is that for $E_x > E_{K\alpha\ filter}$, the filter will fluoresce producing spurious Kα,β X-rays, from the filter material in the detector.

The background continuum observed at the detector will also be modified by the filters. A similar energy dependence to Equation (24) is found. Figure 19 shows the effect of four layers of Perspex (T = 4) on the background produced by a carbon blank.

Perspex filters have been used to:

(i) Eliminate summing peaks. The count rate in a low energy peak is reduced by the filters, hence eliminating the corresponding high energy summing peaks which may interfere with the X-ray region of interest. Figure 33 shows the use of filters for the reduction of summing peaks.

(ii) Reduce the total X-ray count in the low energy region. The electronic deadtime is considerably increased by the high count rates in the lower X-ray energy region. Filters will markedly reduce this deadtime enabling beam currents and aperture sizes to be increased so that a high count rate will be obtained in the higher X-ray energy region. Figure 34 shows this effect.

6. SYSTEM SENSITIVITY

Standard samples of TEG 50B and TEG 50C (supplied by Eastman Kodak Co., Rochester, New York) have been used to measure the system sensitivity versus the Z of the trace element. The samples consist of mixtures of most elements in the Z range 20-50 in a gelatin matrix. The individual elements have concentrations of about 50 μg g^{-1}.

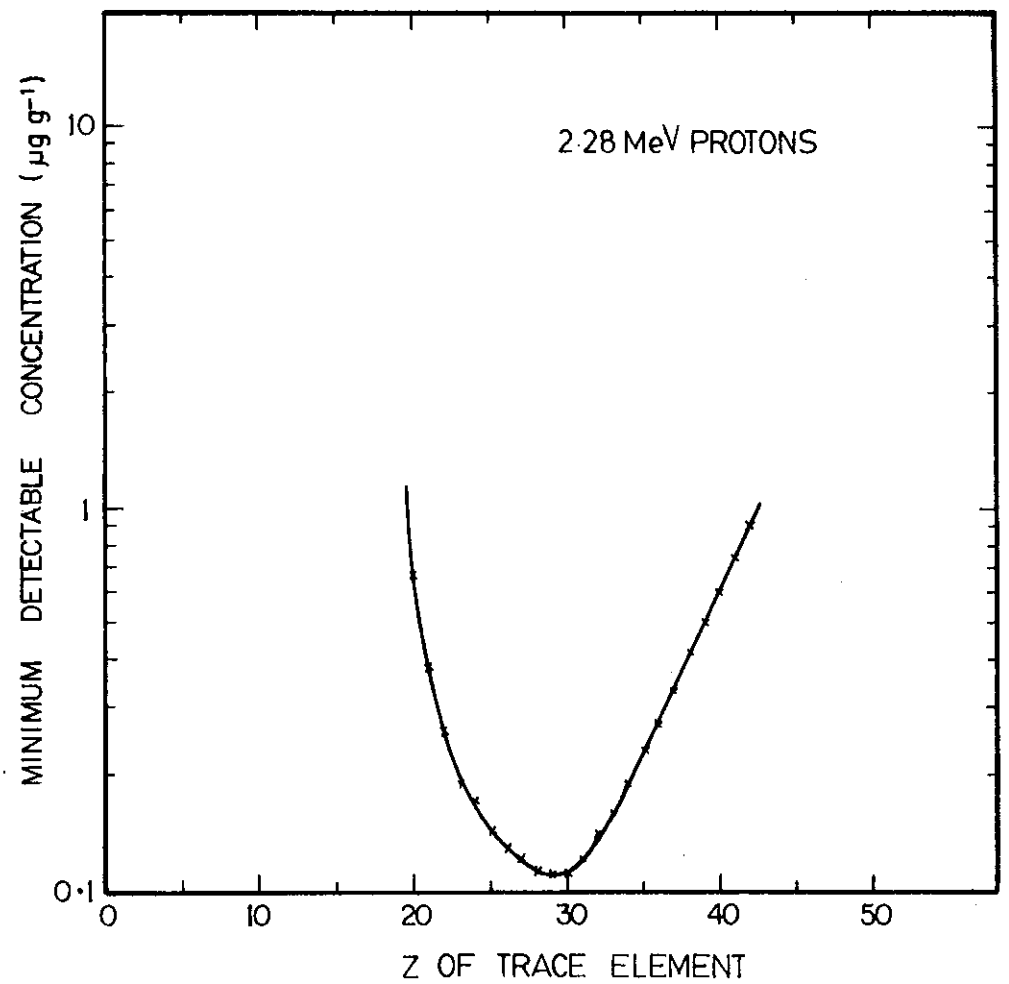

Figure 36 Minimum Detectable Concentration *versus* Z

Figure 17 shows the results for the sample TEG 50C. Background removal and peak analysis have been described by Clayton *et al.* [1978]. The Kα peak counts per μg g^{-1} per 100 μC have been plotted against Z in Figure 35.

A theoretical prediction for the counts per μg g^{-1} per 100 μC versus Z was made from Equation (11):

$$N_T^{approx} = 15\ N_x(It) \left[\frac{C\rho R}{W}\right] [\exp(-2.5 \times 10^{-5}\ \mu\rho R)]\ \Omega\varepsilon\ , \quad (11)$$

where ε, the detector efficiency, is replaced by

$$\varepsilon = \exp[-23/E^3] \quad (25)$$

The above equations were used to calculate N_T per μg g^{-1} per 100 μC for a carbon matrix with proton energy E_p = 2.28 MeV, and are included in Figure 35. There is good agreement between the measured sensitivity of our system and the calculation of sensitivity for a Z range 22-45 for Kα X-rays.

Standard samples for the Lα range of Z are not available. The sensitivities for Th Lα and U Lα have been measured and are described by Cohen *et al.* [1978].

6.1 Minimum Detectable Count

The minimum detectable count in a peak N in a spectrum is defined as

$$N = 3\ \sigma_B$$

where σ_B is the standard deviation of the background under the peak.

Standard deviations of the background below the peak have been calculated from the carbon blank of Figure 25 and the minimum detectable count N is plotted versus Z in Figure 35. For Z between 20 and 40, we certainly have a sensitivity of better than 1 μg g^{-1} per 100 μC. Figure 36 shows the minimum detectable concentration in μg g^{-1} per 100 μC versus Z for Kα X-rays and a proton energy of 2.3 MeV. The minimum value of this curve can be shifted by varying the proton energy E_p; it occurs at a Z value whose Kα X-ray energy is

$$E_x\ (keV) = 1.5\ E_{max} = 3.3\ E_p\ (MeV)\ ,$$

where E_{max} was obtained from Equation (14). The minimum for E_p = 1-3 MeV can be adjusted for the range Z = 19 to 33.

7. CONCLUSION

The fundamental characteristics of the AAEC's PIXE facility at Lucas Heights have been described in full and an approximation has been made for the effective active volume of the target for thick target matrix corrections. Good predictions can now be made for the number of X-rays detected for trace elements in a variety of matrices.

Quantitative analysis of Kα X-rays for elements in the Z range 20-50 has been described and concentrations less than 1 $\mu g\ g^{-1}$ are readily detected if there is no adjacent element interference and if the γ-ray contribution to the background in the region of interest is small.

X-ray filters and electron target flooding have been used to optimise the system sensitivity in selected regions of the X-ray spectrum. Spurious peaks, *e.g.* sum and escape peaks, can be readily recognised and removed during analysis of the spectrum.

Background components in various X-ray energy regions have also been discussed and suggestions to minimise these components and hence improve sensitivity of the system have been made.

The system has been used with great success in the higher energy X-ray region (10-30 keV), *e.g.* for the analysis of uranium and thorium concentrations in ore samples. There are still some minor problems in the lower energy region (0-10 keV) when predicting and subtracting the secondary electron bremsstrahlung background component. Sensitivity in this low energy region should approach the values quoted when better low energy background shapes for Z or an equivalent matrix Z are obtained. For a known matrix, the background is well determined, but for a matrix which is a mixture of light elements, *e.g.* ore samples, the equivalent Z is required. This work is being continued.

The present experimental arrangement works well, but several simple modifications could improve the system:

(1) If the detector were placed inside the chamber, the two beryllium windows and the air gap could be replaced by one beryllium window. The minimum detectable element would then be lowered from silicon to sodium.

(2) The detector resolution of 285 eV at 5.9 keV is not as low as it should be. Detectors with resolution ~ 150 eV are commercially available.

8. ACKNOWLEDGEMENTS

The authors thank A. van Heugten, H. Broe, J.P. Fallon, L.H. Russell and M.J. Kenny for their installation of the target chamber and its ancillary equipment. M.D. Scott and R.J. Cawley assembled and programmed the software for data acquisition; Mr Scott also designed and built the carbon filament and battery needed to overcome the high target potential problem. Thanks are also due to the 3 MeV Van de Graaff accelerator operating staff. This research is partially funded by the Australian Institute of Nuclear Science and Engineering.

9. REFERENCES

Ahlberg, M., Johansson, G. & Malurquist, K. [1975] - *Nucl. Instrum. Methods*, 131 : 377.

Bambynek, W., Grassemann, B., Fink, R.W., Freund, H.U., Mark, H., Swift, C.D., Price, R.E. & Vunngopala Rao, P. [1972] - *Rev. Mod. Phys.*, 44 : 716.

Beech, A.M. & Eberhardt, J.E. [1973] - AAEC/E297.

Charnley, N. [1977] - quoted in Statham, P.J. [1977] as a private communication.

Clayton, E.J., Cohen, D. & Duerden, P. [1978] - AAEC report in preparation.

Cohen, D., Duerden, P. & Clayton, E.J. [1978] - AAEC report in preparation.

Deconninck, C., Demortier, G. & Bodart, F. [1975] - *At. Energy Rev.*, 13 (2) 367.

Flochini, R.G., Feeney, R.J., Sommerville, R.J. & Cahill, T.A. [1972] - *Nucl. Instrum. Methods*, 100 : 397.

Folkmann, F., Gaarde, C., Huns, T. & Kemp, K. [1974a] - *Nucl. Instrum. Methods*, 116 : 487.

Folkmann, F., Borggreen, J. & Kjeldgaard, A. [1974b] - *Nucl. Instrum. Methods*, 119 : 117.

Gordon, B.M. & Kraner, H.W. [1972] - *J. Radioanal. Chem.*, 12 : 181.

Goulding, F.S. [1977] - *Nucl. Instrum. Methods*, 142 : 213.

Johansson, T.B., Akselsson, K. & Johansson, S.A.E. [1970] - *Nucl. Instrum. Methods*, 84 : 141.

Johansson, S.A.E. & Johansson, T.B. [1976] - *Nucl. Instrum. Methods*, 137 : 473-516.

Kaji, H. & Shiokawa, T. [1977] - *Nucl. Instrum. Methods*, 142 : 21.

Kandiah, K. [1973] - Proc. 8th Conf. Electron Probe Analysis Soc. of America, New Orleans, Paper 12.

Kaufmann, H.C. & Akselsson, K.R. [1977] - *Nucl. Instrum. Methods*, 142 : 251.

Musket, R.G. [1974] - *Nucl. Instrum. Methods*, 117 : 385.

Reuter, W., Lurio, A., Cardone, F. & Ziegler, J.F. [1975] - *J. Appl. Phys.*, 46 : 3194.

Scofield, J.H. [1974] - *Phys. Rev. A.*, 9 (3) 1048.

Statham, P.J. [1977] - *X-ray Spectrom.*, 6 (2) 94.

Watson, R.L., McNeal, C.J. & Jensen, F.E. [1975] - *Adv. X-ray Anal.*, 18 : 288.

Woldseth, R. [1975] - X-ray Energy Spectrometry. Kevex Corporation, Burlingame, California, USA.

APPENDIX A

ESTIMATION OF THE TOTAL NUMBER OF X-RAYS PRODUCED BY A THIN AND A THICK TARGET

Let ρ be the density of the matrix,

A_{beam} the proton beam area,

R the proton range in the matrix,

x the thin target thickness,

W the atomic weight of the trace element,

Ω the solid angle subtended at the detector,

It the current x time for total charge hitting the target,

C the fraction by weight of trace element in the matrix,

N_A Avogadro's number,

μ mass absorption coefficient of the matrix, and

N_X number of X-rays produced, $atom^{-1}\ sr^{-1}\ (\mu C\ cm^{-2})^{-1}$.

Then for a thin target

$$\text{Mass of active matrix} = \rho x\ A_{beam}$$

$$\text{Mass of trace element} = C\rho x\ A_{beam}\ ,$$

$$\text{Number of trace element atoms} = \frac{C\rho x\ N_A\ A_{beam}}{W}\ ,$$

$$\text{Number of trace element atoms } cm^{-2} = \frac{C\rho x\ N_A}{W}\ . \qquad \text{(i)}$$

But from Equation (8)

$$N_T^{thin} = AN_X\ (It)\ \Omega\varepsilon\ ,$$

hence

$$N_T^{thin} = \frac{C\rho x\ N_A}{W}\ N_X(It)\ \Omega\varepsilon\ , \qquad \text{(ii)}$$

$$= 600\ N_X\ (It)\ \frac{C}{W}\ \Omega\varepsilon\ , \qquad \text{(iii)}$$

where It is in μC,

C is in $\mu g\ g^{-1}$,

W is in g,

Ω is in steradians,

N_X is in units of $10^{-12}\ atom^{-1}\ sr^{-1}\ (\mu C\ cm^{-2})^{-1}$,

and the thin target thickness ρx is 1 mg cm^{-2}.

For a thick target, the irradiated target volume is $R\ A_{beam}$.

Since 50 per cent of the X-rays are produced in only one quarter of the proton range, it is assumed that the active target volume is only 0.25 R A_{beam}. Further, it is assumed that all the trace element atoms in this active volume occur in a thin layer at a depth R/4 in the target matrix. Hence

$$\text{Mass of active matrix} = \frac{\rho R\, A_{beam}}{4},$$

$$\text{Mass of trace element} = \frac{C\rho R\, A_{beam}}{4},$$

$$\text{Number of trace element atoms per cm}^2 = \frac{C\rho R\, N_A}{4W}. \qquad \text{(iv)}$$

The total number of X-rays produced by this layer is then

$$\left[\frac{C\ R\ N_A}{4W}\right]\ [N_X \Omega\ It].$$

These are then attenuated by the matrix in traversing the distance R/4. Hence

$$N_T^{approx} = \left[\frac{C\rho R\ N_A}{4W}\right]\ [N_X\ \Omega\ It]\ [e^{-\mu\rho\ R/4}]\ \varepsilon, \qquad \text{(v)}$$

is the total number of detected X-rays, where ε is the detector efficiency. If

R is in μm, and

μ is in $cm^2\ g^{-1}$,

Equation (v) becomes

$$N_T^{approx} = 15\ N_X\ (It) \left[\frac{C\rho R}{W}\right]\ [\exp(-2.5 \times 10^{-5}\ \mu\rho R)]\ \Omega\varepsilon \qquad \text{(vi)}$$

and gives an estimate of the total number of X-rays produced by a thick target.